THE ASTROPHYSICAL JOURNAL, 505:50–73, 1998 September 20

NEAR-INFRARED GALAXY COUNTS TO J AND $K \sim 24$ AS A FUNCTION OF IMAGE SIZE[1]

MATTHEW A. BERSHADY[2]
Department of Astronomy, University of Wisconsin, 475 North Charter Street, Madison, WI 53706; mab@astro.wisc.edu and
Department of Astronomy & Astrophysics, Pennsylvania State University

JAMES D. LOWENTHAL[2]
Department of Physics and Astronomy, University of Massachusetts, Amherst, MA 01003; james@velo.phast.umass.edu

AND

DAVID C. KOO
University of California Observatories/Lick Observatory, Department of Astronomy and Astrophysics,
University of California, Santa Cruz, CA 95064; koo@ucolick.org
Received 1997 January 24; accepted 1998 April 22

ABSTRACT

We have used the Keck 10 m telescope to count objects as a function of image size in two high Galactic latitude fields covering 1.5 arcmin^2 and reaching 50% completeness depths of $K = 24$ and $J = 24.5$ for stellar sources. Our counts extend ~ 1 mag deeper in K than those of surveys with other telescopes; complement other Keck surveys in the K-band that provide counts at comparable or shallower depths but that have not utilized image structure; and extend by several magnitudes the J-band counts from brighter surveys using smaller telescopes that cover larger areas. We find the surface density of objects at $K = 23$ to be higher than previously found ($\sim 500{,}000$ mag^{-1} deg^{-2}), but at $K < 22$ to be consistent with other surveys. The slope of the K-band counts ($d \log A/dm = 0.36$) is similar to others near this depth as well as to our own J-band counts (0.35). Counts in the J- and K-bands are both in excess of our empirical no-evolution models for an open universe, with the largest excess observed in J. The counts are a factor of 2 higher than mild-evolution models at J and $K \sim 23$. The slope of the model counts is insensitive to the assumed geometry even in the near-infrared primarily because the model counts are dominated by low-luminosity ($<0.1L^*$) objects at modest redshift ($z < 1$) with small apparent sizes (half-light radii $\leq 0\farcs4$, i.e., $<4\ h_{50}^{-1}$ kpc). The numbers of observed counts rise most steeply for these smaller objects, which dominate the counts fainter than $K = 22.3$ and $J = 23.3$. However, *the greatest excess relative to no-evolution models occurs for the apparently larger objects*, which have a median $J-K$ of ~ 1.5. At these depths, the size and colors of such objects correspond equally well to luminous ($\geq 0.1L^*$) blue galaxies at $1 < z < 4$, or progressively more diffuse, blue, low-luminosity (0.001–$0.1L^*$) galaxies at $z < 1$. The majority of these sources are too faint for spectroscopic measurement. Based on optical colors, we can rule out the possibility that the excess is caused by very low luminosity ($<0.0001L^*$) red galaxies at $z < 0.25$. We also find a deficit of galaxies with red $J-K$ colors corresponding to nonevolving, luminous, early-type (i.e., "red envelope") galaxies at $1 < z < 3$. Even assuming that the deficit is caused by their appearance as blue galaxies, they could account for only 10%–30% of the excess of large, blue galaxies. The nature and redshift distribution of excess large and small galaxy populations at $K = 24$ and $J = 24.5$ remain indeterminate from these data alone.

Subject headings: cosmology: observations — galaxies: evolution — galaxies: photometry — galaxies: statistics — galaxies: structure — infrared: galaxies

1. INTRODUCTION

Near-infrared galaxy counts are considered by some to be a panacea for the study of galaxy evolution and cosmology. One reason is that, compared to counts at optical wavelengths, near-infrared counts are less sensitive to the presently unknown amounts of dust reddening within galaxies, as well as to the uncertain evolution of stellar populations with look-back time. Moreover, in the near-infrared, k-corrections are well known to high redshifts because they are based on well-studied optical photometry of local galaxies (see, e.g., Bershady 1995). However, the flatness of the K-band counts relative to optical counts has been a puzzle that has so far eluded satisfactory—or at least an agreed-upon—explanation (see, e.g., Cowie et al. 1990; Gardner, Cowie, & Wainscoat 1993; Gronwall & Koo 1995; Djorgovski et al. 1995; Yoshii & Peterson 1995). This is because of the difficulty of interpreting galaxy counts (see, e.g., Koo 1990, and references therein), which represent a convolution of a detection function, the multivariate distribution of rest frame galaxy properties (such as luminosity, color, and size), and the cosmological volume. Thus counts alone—even in the near-infrared—are unlikely to provide sufficient information to disentangle these various components and discern the true nature of objects at the faintest limits of observation.

The counts are, however, generally derived from measurements of images, which have the potential to yield additional data. Colors, for example, have been used to infer redshifts beyond the reach of spectroscopy (see, e.g., Lilly, Cowie, & Gardner 1991). Another approach is to exploit image structure at the depths reachable with 4–10 m telescopes (Lilly et al. 1991; Colless et al. 1994), but these efforts

[1] Based on observations obtained at the W. M. Keck Observatory, which is operated jointly by the University of California and the California Institute of Technology.

[2] Previous affiliation: Hubble Fellow, University of California Observatories/Lick Observatory.

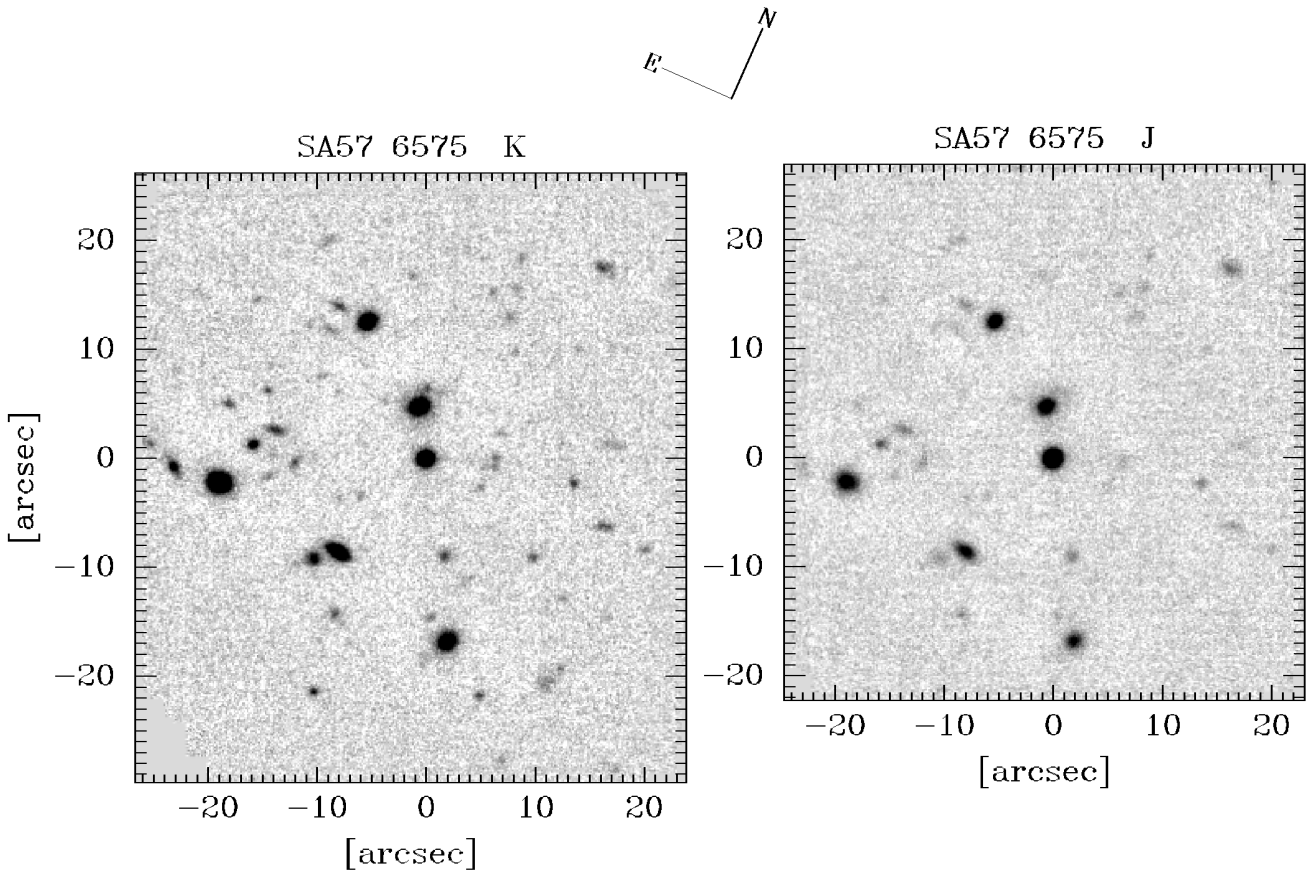

FIG. 1.—K- and J-band images of the SA 57-6575 field at the observed position angle of $-23\overset{\circ}{.}8$. Offsets (in arcseconds) are referenced to the bright, central stellar source SA 57-6575 ($13^h05^m25\overset{s}{.}80$, $+29°33'44\overset{''}{.}3$, 1950), which has V, I, J, K colors consistent with an M4V–M5V star and $K = 17.82 \pm 0.02$ mag. Total exposure times were 20,880 s (K) and 5,940 s (J). Some fraction of data frames were rejected because of unacceptable levels of detector noise. The remaining frames were coadded to maximize the S/N for the reference point source as described in § 3. The resulting useful exposure times are 17,500 s (K) and 5,130 s (J), and the coadded images yield FWHMs of $0\overset{''}{.}54$ (K) and $0\overset{''}{.}78$ (J) for the reference stellar source SA 57-6575. The coadded frames displayed here have been scaled by the square root of their exposure map, which normalizes the noise across the field (and consequently sources appear artificially faint at the edges of the frame). These frames were used with FOCAS for object detection, whereas photometry was done separately using the FOCAS source list on the original coadded frames.

are still in their infancy. With excellent seeing of $0\overset{''}{.}3$–$0\overset{''}{.}6$ routinely obtainable in the near-infrared from the ground, object size, surface-brightness, concentration, and asymmetry can all be measured and added to counts, magnitudes, and colors for constraining models to the faintest limits reachable from the largest telescopes. For example, between redshifts of ~ 0.8 and 3.5, there is little change in apparent size for a given metric size ($<20\%$ change for $0.1 < q_0 < 0.5$). If, in addition, the tight correlation between metric size and luminosity already observed for bright samples of nearby galaxies persists to higher redshift, apparent size and luminosity should be well correlated. In other words, *apparent size can be used to estimate luminosity*.

There are caveats. A significant space-density of low surface brightness galaxies, if they exist, will broaden the observed size-luminosity relation, particularly if they are more readily detected in deep images (see, e.g., Ferguson & McGaugh 1995). Evolution via merging may also alter this relation, as may any wavelength dependence of the observed galaxy size. Nonetheless, faint surveys sample the moderate-redshift universe at very low luminosities inaccessible to brighter surveys. Therefore it is worthwhile to assess whether the faintest sources are predominantly large or small objects. Naively, one might expect that the small objects may represent a class of low-luminosity objects at low to moderate redshifts, missed by brighter surveys, while the larger objects may be luminous galaxies at high redshifts. In contrast, recent evidence appears to indicate that luminous (L^*), high-redshift ($z > 3$) galaxies are predominantly small (Giavalisco, Steidel, & Macchetto 1996; Lowenthal et al. 1997). These measurements, however, have been made in the rest frame ultraviolet for a select sample of galaxies; the near-infrared image structure for complete magnitude-limited samples is not known.

In this paper, we consider these extra dimensions of information by presenting very faint, near-infrared counts in the J- and K-bands as a function of image size from images taken with the Keck 10 m telescope. We have taken advantage of the excellent seeing ($\sim 0\overset{''}{.}6$ FWHM), large telescope aperture, and low backgrounds to obtain very deep, but small (~ 0.7 arcmin^2) images of two high Galactic latitude fields. To assess the nature of the galaxies in our sample, we construct a null hypothesis for the counts and colors as a function of image size at faint magnitudes by adopting a no-evolution model that is based on observations of a brighter, multicolor sample (Bershady et al. 1994). We then determine how the observed counts and size and color distributions deviate from this well-defined prediction. This

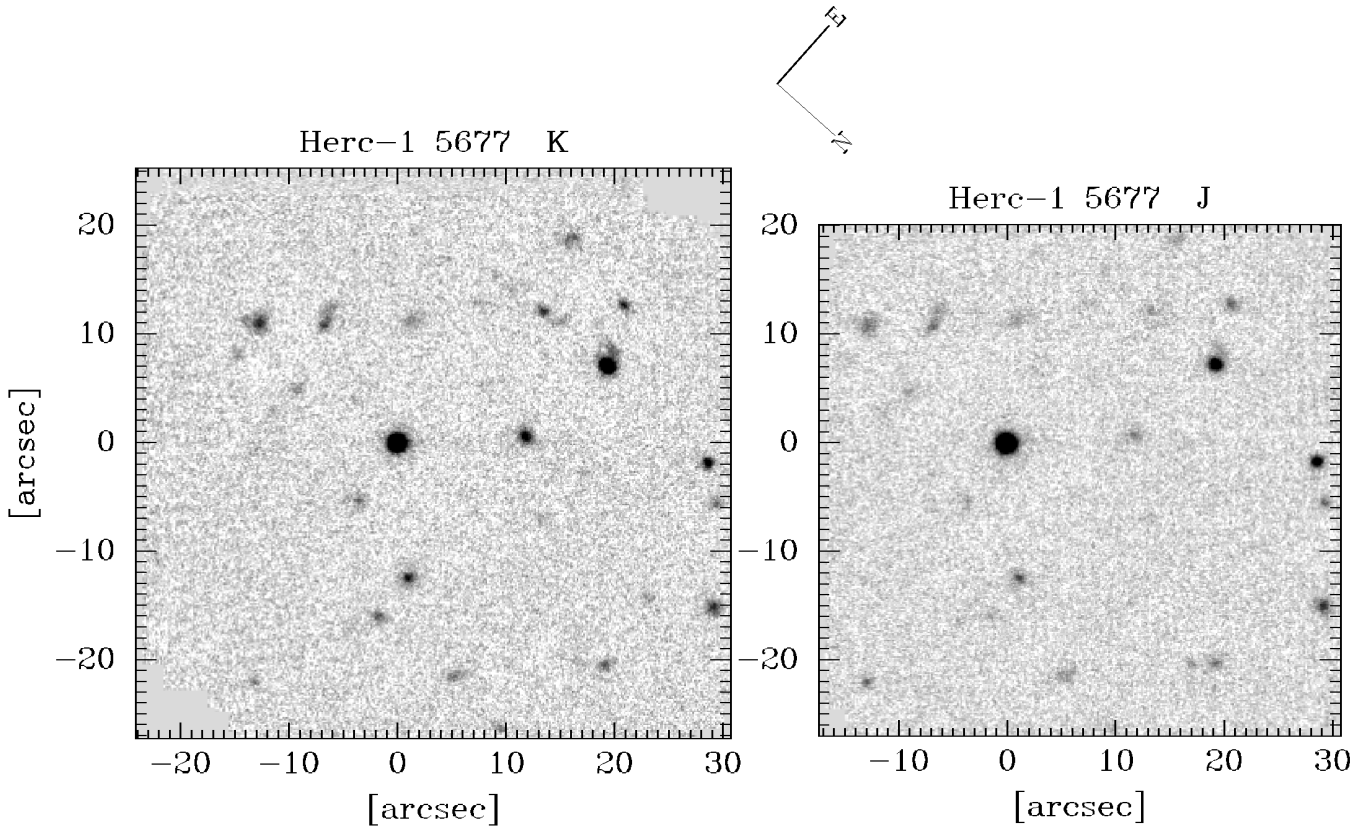

FIG. 2.—*K*- and *J*-band images of the Herc 1-5677 field at the observed position angle of −133°. Offsets (in arcseconds) are referenced to the bright, central stellar source Herc 1-5677 ($17^h19^m43^s.1$, +49°49′47″, 1950), which has *V*, *I*, *J*, *K* colors consistent with a K7V star and $K = 17.42 \pm 0.02$. Total exposure times were 8,910 s (*K*) and 2,970 s (*J*). As for the images in Fig. 1, some fraction of data frames were rejected, and the remaining frames were coadded to maximize the S/N for the reference point source. The resulting useful exposure times are 8,550 s (*K*) and 2,880 s (*J*), and the coadded images yield FWHMs of 0.″64 (*K*) and 0.″66 (*J*) for the reference stellar source Herc 1-5677. The coadded frames displayed here have been scaled by the square root of their exposure map. Object detection and photometry were carried out as described in the legend to Fig. 1 and in the text.

approach has the advantage that it obviates all but cosmological model assumptions. Hence the measured differences between model predictions and observations can be attributed cleanly to failings of the model or to galaxy evolution without recourse to fine-tuning model-specific parameters.

The organization of the paper is as follows: § 2 details our field selection and observations, followed by a description of the image processing (§ 3), object detection (§ 4), and photometry and measurements of counts (§ 5). A data table of sizes and magnitudes for individual sources is presented therein. Our analysis of the observed *J*- and *K*-band counts and model predictions are presented in § 6, while the sizes, colors, and evolution are discussed in § 7. The main findings of our survey are summarized in the concluding § 8. An Appendix contains a description of how counts are derived from images of nonuniform depth

2. FIELD SELECTION AND OBSERVATIONS

Several fields where multiband optical photometry already existed at high Galactic latitudes were chosen for near-infrared imaging. Our two deepest near-infrared fields (Figs. 1 and 2) are SA 57-6575 (part of an area studied by Hall & MacKay 1984 using deep CCD drift scans in two bands similar to *R* and *I*; hereafter SA 57), and Herc 1-5677 (part of an area where deep *U* CCD data have been obtained by Majewski, Koo, & Kron; hereafter Herc 1). Our selection criteria for these fields were (1) that they be centered on a star sufficiently bright to provide accurate registration and point-spread function (PSF) determination, but not too bright to cause problems with scattered light, and (2) that the apparent surface density of faint galaxies as visually assessed in the deep optical CCD data ($R \sim 25$) appeared representative of a much larger region covered in the optical images. We intentionally did not select "blank" fields, since such a choice would bias a survey to sampling systematically underdense lines of sight. This bias could be substantial even at faint magnitudes if low-luminosity galaxies are inherently spatially correlated with more luminous galaxies, which have been "avoided" by selection of "blank" fields.

Observations were conducted in *J*-, *H*-, *K*-, *K*′-, and K_s-bands[3] on three nights (1994 April 24–27) using the Keck I telescope and the Near-Infrared Camera (NIRC).[4] Conditions were almost totally photometric, with seeing ranging from 0.″4–1.″5 FWHM, with a median of 0.″6. Target expo-

[3] Most "standard" *K*-bands cover between ∼2 and 2.4 μm (see, e.g., Bessell & Brett 1988), whereas the *K*′-band (Wainscoat & Cowie 1992) covers between ∼1.9 and 2.3 μm and the K_s- (*K* short) band covers ∼2–2.3 μm. *K*′ and K_s are designed to avoid the rising thermal background at the red end of the *K* window. The possible advantage of *K*′ over K_s is greater bandwidth, but this depends critically on the transparency (and emissivity) of the atmosphere at the blue end of the *K* window. The specific NIRC filter half-power points at 77° K are: 1.105–1.397 μm (*J*), 1.491–1.824 μm (*H*), 2.000–2.427 μm (*K*), 1.955–2.292 μm (*K*′), and 1.99–2.32 μm (K_s).

[4] 256^2 SBRC InSb array, 0.″15 pixel^{-1} (Matthews & Soifer 1994).

sures were 10 s in length, with a dwell time of 90 s per position. A dither sequence of 11 pointings was used, with characteristic offsets of 9″; we also adopted additional random offsets of 1″–3″ between sequences. Typical backgrounds in J and K' were 15.7 ± 0.1 and 13.5 ± 0.1 mag arcsec^{-2}, respectively. Six faint standard stars,[5] covering a range of $-0.22 < J-K < 0.42$ and $-0.14 < H-K < 0.06$, were observed in J-, H-, K-, K'-, and K_s-bands at several exposure times. While most of our target data was observed in the J- and K'-bands,[6] the standard stars and target frames taken in the K-band were used to calibrate directly to the standard K-band. Magnitudes and colors are quoted here in the Vega system. We estimate photometric zeropoint uncertainties to be $\leq 2\%$, but we note that all of the standards were substantially bluer than most of the target sources.

3. IMAGE PROCESSING

Prior to image reduction, a series of images of the warm dome covering a large range of exposure times (and hence detected count levels) were analyzed to determine the linearity of the NIRC response. The resulting curve of count rate versus total counts indicated that, for all applications in this program, the departure from linearity would be less than 1.5% and thus small enough to ignore.

All images were first bias subtracted using "master" bias frames; such frames were constructed from clipped averages of multiple dark frames with minimum integration times (0.43 s). Flat-field calibration images were then constructed for each band on each night by combining (with a median filter) all the unregistered data obtained in that band on that night, and these were used to flatten all the individual data frames. A map of bad (i.e., hot or dead) pixels was assembled by examining the pixel statistics of a large number of images and rejecting those pixels that either varied widely from frame to frame or stood consistently more than 10 σ above or below the mean. A sky image, made from a median of the nine frames closest in time and with the same filter, was subtracted from each frame.

A preliminary image stack was then used to make a mask image that indicates the pixel positions brighter than 2 σ above the sky background. Typically 1%–2% of the total pixels in the image were included in the mask image. The sky subtraction was repeated on each original frame, using the mask to exclude bright objects from each individual sky image before building the composite sky frame. Bad pixels and pixels previously flagged as affected by cosmic rays were also excluded. This initial data reduction used the software package DIMSUM within IRAF (Stanford et al. 1995).

The flatness of the individual processed images was found to be a few times 10^{-5} of the sky on scales of 15″–35″. To remove these small remaining gradients, a second sky subtraction was performed using a first-order cubic spline fit to the unmasked pixels of each image. A final image stack for each field and band was made by first registering all images via cross correlation of the brightest 6–10 objects and then weighting each image by the signal-to-noise ratio (S/N) of the bright central star as determined from multiaperture photometry in each image. The S/N was defined to be proportional to the ratio of the photon counts within the half-light radius to the effective sky noise within the half-light radius (close to the maximum S/N). In this way, the S/N explicitly took into account changes in seeing, transparency, and background. The weighting process substantially improved the image depth and quality, with the final flatness over large scales being $< 3 \times 10^{-6}$ of the sky. For object detection with the Faint Object Classification and Analysis System (FOCAS) (but not for photometry; see below), the final image stacks were scaled by the square root of the exposure maps to normalize the noise to a constant value across the image (as displayed in Figs. 1 and 2).

4. OBJECT DETECTION

There is always a trade-off between completeness, which we define as the depth where 50% of the objects are detected) and reliability (percentage of real vs. spurious detections) at that depth. If the reliability function can be accurately determined, object detection can be pushed to fainter limits by relaxing the detection criteria to improve completeness. In practice, reliability is difficult to measure unless one has additional (and preferably deeper) data to make an independent assessment. Since we are pushing to the very faintest limits at high backgrounds, unknown sources of electronic noise and known (but poorly characterized) imperfect camera baffling both led us to be cautious and choose detection parameters that minimized spurious detections.

Completeness and reliability also depend on the image structure of the objects. Smaller or more concentrated (higher surface brightness) objects are more readily detected at a given total magnitude, but spurious detections tend to be more frequent. In addition to being interested in counting sources as a function of image size, we are compelled to do so simply in order to estimate correctly the total number of sources.

We have used FOCAS (Jarvis & Tyson 1981; Valdes 1982) to detect sources. We have also tested the completeness and reliability as a function of the FOCAS detection parameters: minimum area, isophotal threshold, and detection kernel. For a grid in this parameter space, we determined detection completeness as a function of total magnitude and image size (defined below), using $\sim 10^4$ simulations for each of the four final, stacked images. Test sources consisted of the brightest six objects in both fields ($K < 19$) that spanned the observed range of image size, including the PSF. These templates were artificially dimmed and added back into the original images at random locations. FOCAS was then run with the same detection parameters to search for the simulated objects. As expected, the completeness scaled with the square root of the effective exposure time.

Detection reliability was measured by photometering all detected objects on a pair of images constructed from each of two randomly chosen but exclusive halves of the data (for each field and band) in circular apertures equivalent to the isophotal area as detected in the full image stacks. Objects with magnitudes differing by more than 5 σ (as determined by the sky noise and photometry aperture) were considered to be spurious detections. When the detection parameters yielded few such deviant points, the distribution of magnitude differences appeared bimodal, and visual inspection of the "spurious" detections nominally confirmed the numerical result. The reliability in this case is a steeply dropping

[5] FS 15, 21, 20, 19, 27, and 33, (Casali & Hawarden 1992).

[6] K' yielded the highest signal-to-noise ratio, compared to K or K_s, which had backgrounds of $13.6^{+0.1}_{-0.35}$ and 13.75 ± 0.1 mag arcsec^{-2}, respectively.

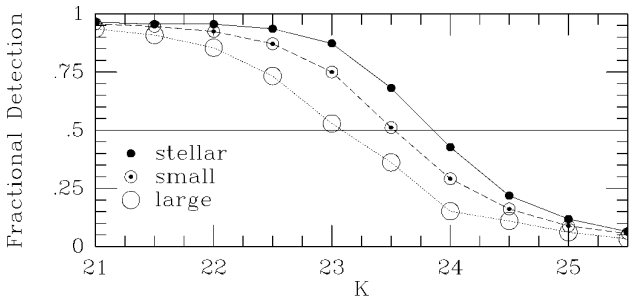

FIG. 3.—Fractional detection as a function of total K-magnitude and image size for the deepest image (SA 57-6575 field; Fig. 1). Total magnitudes and sizes for "small" and "large" are defined in the text. The lower limiting case ("stellar") has a 50% detection limit (m_{50}) roughly 0.4 mag fainter than for the average "small" source.

function of flux, beginning near the 50% completeness limit. With detection parameters yielding larger numbers of deviant points, the bimodality disappeared; similarly it became difficult to assess detection reliability visually. Such detection parameters were excluded from further consideration. It is worth noting that additional simulations showed that reliability would be substantially *overestimated* by counting sources detected in simulated blank Gaussian random-noise fields. This method was adopted by Djorgovski et al. (1995).

Based on the above tests, we chose a $+3/-6\ \sigma$ isophotal threshold, a minimum area corresponding to that within the FWHM of the PSF in each image, and the PSF as the detection kernel. This set is optimal for detecting unresolved sources. In addition to the quantitative estimates of completeness and reliability, we visually inspected the images to check that the chosen parameters appeared to detect all apparently real objects, while minimizing the number of spurious detections. The isophotal threshold corresponds to surface brightnesses in the kernel-convolved images of 24.25, 25.5, 23.9, and 25.0 mag arcsec^{-2} for the deepest regions of SA 57 K and J and Herc 1 K and J, respectively. These numbers are indicative of our ability to detect large, low surface brightness objects. More relevant for the detection of compact sources are the magnitudes corresponding to the 3 σ detection limits for flux within the minimum detection area. These correspond to 25.1, 25.8, 24.5, and 25.5 mag, again for the deepest regions of SA 57 K and J and Herc 1 K and J, respectively. The S/N at 50% detection limits, however, is around 5, independent of image size.

Figure 3 illustrates the completeness as a function of K-magnitude and image size for the deepest portion of the SA 57-6575 field. Table 1 lists, in brackets in each heading, (1) the 50% detection limits for each object image size and (2) the reliability at these limits. Note that the difference in

TABLE 1

DIFFERENTIAL COUNTS AS A FUNCTION OF IMAGE SIZE

	SA 57-6575				Herc 1-5677			
	s (SMALL) K = [23.5, 0.88] J = [24.1, 0.92]		l (LARGE) K = [23.1, 1.00] J = [23.7, 0.75]		s (SMALL) K = [23.0, 0.50] J = [23.8, 0.80]		l (LARGE) K = [22.6, 0.88] J = [23.3, 1.00]	
MAGNITUDE	N	log A	N	log A	N	log A	N	log A
				K				
18.50	2	$3.97^{+0.37}_{-0.45}$	2	$3.98^{+0.37}_{-0.45}$	1	$3.67^{+0.52}_{-0.76}$	0	...
19.00	0	...	2	$3.98^{+0.37}_{-0.45}$	1	$3.67^{+0.52}_{-0.76}$	1	$3.68^{+0.52}_{-0.76}$
19.50	0	...	4	$4.29^{+0.25}_{-0.28}$	1	$3.67^{+0.52}_{-0.76}$	4	$4.30^{+0.25}_{-0.28}$
20.00	2	$4.00^{+0.37}_{-0.45}$	5	$4.40^{+0.22}_{-0.25}$	5	$4.39^{+0.22}_{-0.25}$	4	$4.31^{+0.25}_{-0.28}$
20.50	3	$4.18^{+0.29}_{-0.34}$	7	$4.58^{+0.19}_{-0.20}$	7	$4.54^{+0.19}_{-0.20}$	5	$4.44^{+0.22}_{-0.25}$
21.00	8	$4.64^{+0.17}_{-0.19}$	8	$4.66^{+0.17}_{-0.19}$	5	$4.42^{+0.22}_{-0.25}$	6	$4.54^{+0.20}_{-0.22}$
21.50	12	$4.84^{+0.14}_{-0.15}$	9	$4.78^{+0.16}_{-0.17}$	4	$4.36^{+0.25}_{-0.28}$	6	$4.66^{+0.20}_{-0.22}$
22.00	12	$4.89^{+0.14}_{-0.15}$	11	$4.92^{+0.15}_{-0.15}$	8	$4.81^{+0.18}_{-0.20}$	8	$4.93^{+0.18}_{-0.19}$
22.50	22	$5.24^{+0.10}_{-0.11}$	10	$5.03^{+0.16}_{-0.17}$	11	$5.05^{+0.16}_{-0.18}$	6	$4.96^{+0.21}_{-0.23}$
23.00	31	$5.52^{+0.09}_{-0.11}$	11	$5.24^{+0.15}_{-0.17}$	8	$5.15^{+0.19}_{-0.25}$	...	...
23.50	37	$5.80^{+0.12}_{-0.16}$	...	...	...	...	...	...
				J				
19.50	1	$3.75^{+0.52}_{-0.76}$	2	$4.05^{+0.37}_{-0.45}$	1	$3.76^{+0.52}_{-0.76}$	0	...
20.00	2	$4.05^{+0.37}_{-0.45}$	4	$4.35^{+0.25}_{-0.28}$	2	$4.07^{+0.37}_{-0.45}$	1	$3.77^{+0.52}_{-0.76}$
20.50	1	$3.75^{+0.52}_{-0.76}$	2	$4.05^{+0.37}_{-0.45}$	1	$3.77^{+0.52}_{-0.76}$	2	$4.09^{+0.37}_{-0.45}$
21.00	0	...	1	$3.81^{+0.52}_{-0.76}$	1	$3.80^{+0.52}_{-0.76}$	2	$4.11^{+0.37}_{-0.45}$
21.50	1	$3.79^{+0.52}_{-0.76}$	5	$4.53^{+0.22}_{-0.25}$	4	$4.41^{+0.25}_{-0.28}$	5	$4.54^{+0.22}_{-0.25}$
22.00	1	$3.79^{+0.52}_{-0.76}$	6	$4.62^{+0.20}_{-0.22}$	6	$4.60^{+0.20}_{-0.22}$	8	$4.78^{+0.17}_{-0.19}$
22.50	3	$4.34^{+0.30}_{-0.34}$	10	$4.93^{+0.16}_{-0.16}$	6	$4.64^{+0.20}_{-0.22}$	7	$4.79^{+0.19}_{-0.20}$
23.00	9	$4.88^{+0.17}_{-0.18}$	11	$5.03^{+0.15}_{-0.16}$	7	$4.78^{+0.19}_{-0.21}$	6	$4.88^{+0.20}_{-0.23}$
23.50	15	$5.24^{+0.14}_{-0.16}$	9	$5.16^{+0.17}_{-0.18}$	16	$5.36^{+0.16}_{-0.22}$	3	$4.67^{+0.30}_{-0.36}$
24.00	19	$5.50^{+0.14}_{-0.18}$	...	...	26	$5.78^{+0.16}_{-0.26}$	...	...

NOTES.—N denotes raw counts as detected in each image; log A denotes the log of the corrected counts mag^{-1} deg^{-2}. Square brackets contain the magnitudes (m_{50}) at which counts are 50% complete and the fraction of reliable detections within $m_{50} \pm 0.25$ mag. Image sizes for each class, s (small) and l (large), in each field are defined in the text.

TABLE 2

SOURCE CATALOG

ID (1)	Δx (2)	Δy (3)	J (4)	$\sigma(J)$ (5)	K (6)	$\sigma(K)$ (7)	$\theta_{0.5}$ (8)	$\sigma(\theta)$ (9)	C (10)	S (11)
SA 57-6575 Field[a,b]										
sk144[c]	0.0	0.0	18.69	0.05	17.82	0.03	0.42	0.00	*s*	*J*, *K*
sk118	−19.2	−2.2	19.67	0.05	17.82	0.03	0.79	0.01	*l*	*J*, *K*
sk148	−0.6	4.8	19.84	0.05	18.21	0.03	0.57	0.00	*s*	*J*, *K*
sk189	−5.3	12.7	20.08	0.05	18.39	0.03	0.52	0.00	*s*	*J*, *K*
sk050	1.9	−17.0	20.16	0.05	18.42	0.03	0.63	0.01	*l*	*J*, *K*
sk070	−8.1	−8.6	20.44	0.05	18.54	0.03	0.65	0.01	*l*	*J*, *K*
sk120	−23.2	−0.7	21.60	0.06	19.33	0.04	0.64	0.03	*l*	*J*, *K*
sk113	−25.5	1.4	...	...	19.57	0.04	0.90	0.21	*l*	*K*
sk007	7.1	−28.0	...	...	19.89	0.06	0.81	0.28	*l*	*K*
sk071	−10.4	−9.2	21.99	0.06	19.93	0.03	0.80	0.02	*l*	*J*, *K*
sk123	−16.0	1.3	21.95	0.06	20.25	0.03	0.47	0.01	*s*	*J*, *K*
sk003	17.6	−28.9	...	...	20.26	0.09	0.54	0.22	*s*	*K*
sk214	16.4	17.6	21.47	0.06	20.41	0.07	0.73	0.03	*l*	*J*, *K*
sk201[e]	23.0	16.5	21.7	0.1	20.44	0.06	1.00	0.40	*l*	*K*
sk122	−13.8	2.7	21.98	0.06	20.54	0.04	0.72	0.03	*l*	*J*, *K*
sk029	11.2	−21.0	23.55	...	20.67	0.11	0.96	0.19	*l*	*K*
sk021	−10.2	−21.5	22.42	0.13	20.68	0.10	0.43	0.04	*s*	*K*
sk065	1.8	−9.0	22.15	0.06	20.95	0.04	0.63	0.03	*l*	*J*, *K*
sk190	−7.9	14.2	22.59	0.07	20.97	0.06	0.72	0.05	*l*	*J*, *K*
sk074	16.7	−6.3	22.65	0.10	20.97	0.08	0.70	0.07	*l*	*J*, *K*
sk018	5.0	−22.0	23.21	...	21.03	0.13	0.54	0.05	*s*	*K*
sk044	−8.4	−14.4	22.59	0.13	21.08	0.05	0.62	0.06	*s*	*J*, *K*
sk110	−12.0	−0.3	22.38	0.07	21.13	0.05	0.70	0.07	*l*	*J*, *K*
sk087	13.8	−2.3	22.85	0.09	21.15	0.06	0.48	0.03	*s*	*J*, *K*
sk135	−18.1	5.0	23.10	0.18	21.34	0.08	0.54	0.05	*s*	*J*, *K*
sk067	10.0	−9.1	24.93	...	21.35	0.06	0.61	0.06	*s*	*K*
sk068	20.3	−8.4	23.17	0.15	21.42	0.11	0.56	0.10	*s*	*J*, *K*
sk227	−9.2	20.1	23.98	0.59	21.43	0.15	0.66	0.15	*l*	*K*
sk030	12.4	−19.5	24.24	...	21.47	0.16	0.66	0.23	*l*	*K*
sk011	14.0	−25.7	...	...	21.48	0.22	0.36	0.40	*s*	*K*
sk202	22.4	15.8	21.82	0.07	21.55	0.17	0.87	0.22	*l*	*J*, *K*
sk187	−8.9	12.2	23.17	0.11	21.59	0.07	0.83	0.16	*l*	*J*, *K*
sk114	−25.3	2.6	...	...	21.62	0.14	0.59	0.55	*s*	*K*
sk241	3.9	24.0	24.51	...	21.70	0.17	0.59	0.61	*s*	*K*
sk194	7.7	13.3	22.92	0.09	21.72	0.07	0.90	0.18	*l*	*J*, *K*
sk100	17.1	1.3	22.74	0.13	21.79	0.22	0.77	0.20	*l*	*J*, *K*
sk221	8.9	18.6	23.54	0.18	21.80	0.19	0.60	0.14	*s*	*J*, *K*
sk099	17.4	1.1	22.74	0.13	21.83	0.17	0.64	0.15	*l*	*J*, *K*
sk147	1.3	6.1	22.64	0.11	21.83	0.11	0.63	0.13	*l*	*J*, *K*
sk138	−14.6	6.3	25.23	...	21.92	0.08	0.52	0.12	*s*	*K*
sk093	6.4	−0.1	22.89	0.09	21.95	0.07	0.61	0.12	*s*	*J*, *K*
sk160	−24.9	9.5	...	...	22.01	0.18	0.30	0.22	*s*	*K*
sk048	0.4	−14.7	23.28	0.24	22.03	0.17	0.68	0.17	*l*	*J*, *K*
sk094	6.4	−0.5	22.89	0.09	22.04	0.10	0.37	0.08	*s*	*J*, *K*
sk109	−14.7	−1.7	23.63	0.16	22.16	0.09	0.64	0.15	*l*	*J*, *K*
sk204	−1.1	17.1	23.39	0.19	22.16	0.14	0.61	0.15	*s*	*J*, *K*
sk197	8.5	15.9	22.81	0.11	22.17	0.12	0.67	0.15	*l*	*J*, *K*
sk193	6.2	15.3	23.08	0.10	22.18	0.12	0.57	0.12	*s*	*J*, *K*
sk115	−14.2	0.5	23.82	0.17	22.30	0.10	0.92	0.38	*l*	*J*, *K*
sk056	12.7	−12.9	23.91	0.25	22.40	0.13	0.50	0.14	*s*	*J*, *K*
sk020	−8.9	−22.6	...	...	22.41	0.46	0.29	0.19	*s*	*K*
sk223	3.9	19.3	24.24	0.35	22.47	0.37	0.36	0.11	*s*	*J*, *K*
sk188	−10.9	12.3	24.19	0.23	22.49	0.15	0.65	0.22	*l*	*K*
sk091	4.9	−2.5	23.86	0.16	22.53	0.11	0.43	0.11	*s*	*J*, *K*
sk066	3.9	−11.1	23.80	0.17	22.57	0.12	0.68	0.24	*l*	*J*, *K*
sk191	−15.6	14.8	23.40	0.16	22.57	0.17	0.54	0.14	*s*	*J*, *K*
sk126	13.6	4.9	24.94	...	22.63	0.19	0.42	0.28	*s*	*K*
sk082	−6.1	−3.5	24.29	0.22	22.63	0.12	0.52	0.11	*s*	*J*, *K*
sk041	17.1	−14.6	23.79	0.38	22.64	0.35	0.47	0.22	*s*	*J*, *K*
sk152	−9.8	7.6	25.17	...	22.67	0.14	0.50	0.12	*s*	*K*
sk175	−16.9	12.8	24.84	...	22.71	0.22	0.48	0.28	*s*	*K*
sk045[f]	−7.7	−15.2	24.99	...	22.72	0.24	<0.6	0.00	*s*	*K*
sk080	−7.9	−3.6	23.85	0.16	22.76	0.14	0.67	0.19	*l*	*J*, *K*
sk167	14.2	10.2	24.20	0.26	22.78	0.18	0.51	0.14	*s*	*J*, *K*
sk222	2.0	19.4	24.99	...	22.81	0.44	0.40	0.42	*s*	*K*
sk146	−3.5	5.5	23.69	0.15	22.83	0.14	0.66	0.18	*l*	*J*, *K*
sk111	−10.4	0.3	25.26	...	22.84	0.14	0.93	0.47	*l*	*K*
sk049	−0.3	−19.0	24.61	...	22.87	0.57	0.44	0.15	*s*	*K*
sk164	8.3	9.9	24.32	0.24	22.88	0.16	0.48	0.15	*s*	*J*, *K*
sk157	−14.3	8.7	23.72	0.22	22.90	0.18	0.59	0.40	*s*	*K*

TABLE 2—*Continued*

ID (1)	Δx (2)	Δy (3)	J (4)	$\sigma(J)$ (5)	K (6)	$\sigma(K)$ (7)	$\theta_{0.5}$ (8)	$\sigma(\theta)$ (9)	C (10)	S (11)
sk101	6.9	2.4	25.25	...	22.91	0.15	0.68	0.35	*l*	*K*
sk098	16.8	2.6	24.68	...	22.91	0.46	0.41	0.42	*s*	*K*
sk112	−12.1	1.5	25.25	...	22.97	0.17	0.27	0.25	*s*	*K*
sk176	−19.4	12.9	24.82	...	23.00	0.40	0.35	0.37	*s*	*K*
sk105	14.9	4.0	24.86	...	23.03	0.29	0.11	0.12	*s*	*K*
sk173	−2.8	11.7	25.88	0.04	23.04	0.26	0.65	0.26	*l*	*K*
sk069	−6.0	−8.3	25.25	...	23.09	0.24	0.76	0.33	*l*	*K*
sk052	11.2	−13.8	24.78	0.58	23.10	0.22	0.36	0.26	*s*	*K*
sk162	11.7	9.1	24.57	0.31	23.11	0.21	0.39	0.28	*s*	*K*
sk090	4.2	0.0	24.18	0.21	23.12	0.18	0.71	0.37	*l*	*K*
sk028	13.4	−18.8	24.61	...	23.13	0.50	0.35	0.37	*s*	*K*
sk145	−1.5	2.6	25.26	...	23.14	0.33	0.68	0.59	*l*	*K*
sk149	0.2	6.5	25.25	...	23.15	0.38	1.49	1.55	*l*	*K*
sk139	−0.6	−2.2	25.26	...	23.16	0.23	0.99	1.03	*l*	*K*
sk064	−18.4	−8.7	24.81	...	23.20	0.44	0.25	0.09	*s*	*K*
sk169	17.4	10.1	25.98	1.16	23.21	0.47	0.49	0.18	*s*	*K*
sk097	12.6	1.4	25.24	...	23.22	0.22	0.36	0.18	*s*	*K*
sk171	−20.8	11.4	24.74	...	23.22	0.47	0.40	0.54	*s*	*K*
sk181	3.7	13.1	25.18	...	23.30	0.25	0.54	0.50	*s*	*K*
sk184	2.8	14.1	25.19	...	23.40	0.28	0.34	0.30	*s*	*K*
sk038	11.5	−16.5	24.88	...	23.42	0.38	0.24	0.21	*s*	*K*
sk226	−12.0	20.1	25.04	...	23.44	0.68	0.47	0.33	*s*	*K*
sk025	−12.6	−19.8	24.33	...	23.44	0.74	0.41	0.45	*s*	*K*
sk107	−13.5	3.8	25.25	...	23.44	0.31	0.30	0.31	*s*	*K*
sk205	0.0	16.2	23.58	0.17	23.48	0.35	0.29	0.27	*s*	*K*
sk198	8.9	15.0	25.26	...	23.52	0.31	0.28	0.32	*s*	*K*
sk209	2.2	17.7	25.20	...	23.56	0.48	0.18	0.19	*s*	*K*
sk103	9.6	3.4	25.25	...	23.56	0.27	0.26	0.09	*s*	*K*
sk142	2.9	7.3	25.25	...	23.57	0.26	0.31	0.18	*s*	*K*
sk196	6.4	12.8	25.25	...	23.57	0.39	0.21	0.12	*s*	*K*
sk183	2.7	12.7	25.26	...	23.62	0.30	0.52	0.57	*s*	*K*
sk220	−12.9	18.7	25.11	...	23.63	0.70	0.33	0.15	*s*	*K*
sk140	1.3	−2.3	25.26	...	23.67	0.27	0.26	0.27	*s*	*K*
sk216	5.3	18.6	25.14	...	23.68	0.67	0.30	0.20	*s*	*K*
sk037	−9.8	−16.8	24.85	...	23.69	0.45	0.40	0.18	*s*	*K*
sk141	2.0	−2.0	25.26	...	23.71	0.28	0.41	0.36	*s*	*K*
sk088	12.4	−2.5	25.26	...	23.75	0.35	0.17	0.23	*s*	*K*
sk072	5.8	−6.3	25.25	...	23.75	0.30	0.40	0.34	*s*	*K*
sk076	0.2	−4.6	25.26	...	23.77	0.30	0.41	0.45	*s*	*K*
sk104	11.9	3.7	25.25	...	23.78	0.34	0.18	0.20	*s*	*K*
sk155	9.7	8.7	25.25	...	23.79	0.33	0.32	0.23	*s*	*K*
sk085	12.6	0.0	25.26	...	23.81	0.35	0.27	0.31	*s*	*K*
sk061	−4.9	−10.1	25.26	...	23.85	0.33	0.42	0.18	*s*	*K*
sk054	6.2	−13.2	25.15	...	23.88	0.37	0.49	0.14	*s*	*K*
sk063	−0.1	−9.5	25.25	...	23.94	0.39	0.20	0.27	*s*	*K*
sk166	−12.1	10.4	25.26	...	23.94	0.39	0.31	0.33	*s*	*K*
sj047	22.4	3.8	23.11	0.14	22.86	...	0.40	0.38	*s*	*J*
sj064	0.1	2.2	23.12	0.26	24.07	...	1.33	0.61	*l*	*J*
sj011	16.6	−15.9	23.55	0.42	23.45	...	0.40	0.42	*s*	*J*
sj115	13.6	22.1	23.60	0.33	22.64	...	0.25	0.18	*s*	*J*
sj018	1.6	−14.8	23.62	0.40	24.13	0.72	0.73	0.64	*l*	*J*
sj015	0.6	−13.1	23.79	0.21	23.99	...	0.42	0.28	*s*	*J*
sj103	−18.2	17.6	23.80	0.29	23.62	0.66	0.45	0.30	*s*	*J*
sj053	13.4	7.0	23.90	0.24	23.76	...	0.49	0.43	*s*	*J*
sj074	10.9	8.8	24.06	0.24	23.88	...	0.30	0.27	*s*	*J*
sj065	−8.2	6.3	24.07	0.19	24.13	0.41	0.41	0.21	*s*	*J*
sj021	0.3	−11.4	24.08	0.22	24.07	...	0.39	0.37	*s*	*J*
sj041	15.8	−0.7	24.10	0.31	23.80	...	0.26	0.13	*s*	*J*
sj030	6.0	−6.9	24.16	0.22	24.00	...	0.27	0.16	*s*	*J*
sj025	8.4	−9.7	24.25	0.24	24.05	...	0.60	0.63	*s*	*J*
Herc 1-5677 Field[a, b]										
hk066[d]	0.0	0.0	18.18	0.05	17.44	0.02	0.51	...	*s*	*J*, *K*
hk086	19.5	7.3	20.14	0.05	18.41	0.02	0.63	0.01	*s*	*J*, *K*
hk058	28.9	−1.7	19.97	0.05	19.15	0.02	0.54	0.01	*s*	*J*, *K*
hk029	29.5	−15.2	20.27	0.05	19.16	0.02	0.75	0.03	*l*	*J*, *K*
hk067	11.9	0.7	21.74	0.06	19.57	0.02	0.79	0.04	*l*	*J*, *K*
hk091[g]	−12.9	11.0	20.85	0.06	19.59	0.04	0.98	0.05	*l*	*J*, *K*
hk124[e]	16.5	19.1	21.4	0.1	19.83	0.09	0.81	0.07	*l*	*K*
hk081	−23.5	8.3	...	...	20.04	0.11	0.38	0.36	*s*	*K*
hk034	1.1	−12.5	21.51	0.05	20.06	0.03	0.69	0.03	*s*	*J*, *K*
hk046	29.7	−5.7	21.23	0.06	20.22	0.04	0.71	0.08	*l*	*J*, *K*

TABLE 2—*Continued*

ID (1)	Δx (2)	Δy (3)	J (4)	$\sigma(J)$ (5)	K (6)	$\sigma(K)$ (7)	$\theta_{0.5}$ (8)	$\sigma(\theta)$ (9)	C (10)	S (11)
hk001	9.8	−26.6	22.32	0.09	20.32	0.06	0.61	0.17	*s*	*J*, *K*
hk099[g]	−6.8	10.9	21.69	0.08	20.39	0.05	0.68	0.04	*s*	*J*, *K*
hk098	21.1	12.9	21.62	0.08	20.42	0.07	0.60	0.03	*s*	*J*, *K*
hk092	13.5	12.3	22.03	0.10	20.58	0.05	0.61	0.07	*s*	*J*, *K*
hk008	5.2	−21.6	22.23	0.16	20.71	0.08	0.78	0.16	*l*	*J*, *K*
hk090	1.1	11.4	21.84	0.08	20.73	0.06	1.00	0.16	*l*	*J*, *K*
hk007	−13.2	−22.2	21.35	0.07	20.77	0.14	0.53	0.07	*s*	*J*, *K*
hk012	19.4	−20.5	21.66	0.08	20.79	0.08	0.72	0.08	*l*	*J*, *K*
hk023	−1.6	−16.1	22.74	0.11	20.85	0.06	0.71	0.10	*l*	*J*, *K*
hk047	−3.6	−5.3	22.40	0.10	21.04	0.06	0.89	0.17	*l*	*J*, *K*
hk083	−14.7	7.9	22.72	0.18	21.26	0.15	0.67	0.14	*s*	*J*, *K*
hk077	−20.0	6.1	...	...	21.42	0.22	0.37	0.32	*s*	*K*
hk073	−9.3	4.8	22.27	0.14	21.44	0.10	0.80	0.19	*l*	*J*, *K*
hk102	10.7	14.3	23.52	0.27	21.46	0.15	0.51	0.11	*s*	*J*, *K*
hk093	15.4	11.2	24.64	...	21.54	0.09	1.09	0.38	*l*	*K*
hk026	23.3	−14.2	24.50	...	21.58	0.14	0.90	0.36	*l*	*K*
hk059	−13.1	−0.7	23.78	...	21.63	0.22	0.80	0.37	*l*	*K*
hk106	26.4	15.6	23.96	...	21.72	0.32	0.49	0.35	*s*	*K*
hk024	−4.4	−17.4	24.34	...	21.87	0.19	0.97	0.45	*l*	*K*
hk013	17.3	−20.5	22.81	0.14	22.00	0.25	0.65	0.19	*s*	*J*, *K*
hk103	11.5	14.8	24.26	...	22.01	0.23	0.79	0.40	*l*	*K*
hk060	−13.7	−1.0	23.93	...	22.02	0.28	0.38	0.25	*s*	*K*
hk038	13.4	−6.9	23.69	0.21	22.13	0.14	0.68	0.20	*s*	*J*, *K*
hk096	7.3	13.1	24.45	...	22.23	0.19	0.39	0.18	*s*	*K*
hk069	−11.5	2.9	22.49	0.17	22.25	0.25	1.16	0.37	*l*	*J*, *K*
hk120	−8.7	18.8	23.81	...	22.29	0.47	0.61	0.29	*s*	*K*
hk068	10.8	−0.2	24.35	...	22.30	0.36	1.81	1.57	*l*	*K*
hk108	9.0	15.6	23.18	0.23	22.43	0.30	0.80	0.29	*l*	*J*, *K*
hk055	14.8	−2.4	24.53	...	22.46	0.20	0.66	0.44	*s*	*K*
hk097	8.1	12.1	24.59	...	22.48	0.22	0.52	0.45	*s*	*K*
hk053	17.3	−2.8	24.67	...	22.53	0.20	0.82	0.38	*l*	*K*
hk048	−4.8	−5.4	24.67	...	22.59	0.22	0.71	0.66	*l*	*K*
hk100	−3.6	10.9	24.67	...	22.71	0.30	0.24	0.22	*s*	*K*
hk070	−4.0	4.1	24.67	...	22.74	0.23	0.56	0.26	*s*	*K*
hk111	2.7	16.6	24.19	...	22.87	0.52	0.56	0.28	*s*	*K*
hk071	7.9	5.4	24.36	0.35	22.89	0.25	0.61	0.21	*s*	*K*
hk075	−3.3	5.5	24.67	...	23.04	0.29	0.26	0.27	*s*	*K*
hk076[f]	17.5	6.6	24.67	...	23.04	1.16	<0.7	...	*s*	*K*
hk072	8.5	5.7	23.84	0.23	23.11	0.30	0.69	0.40	*s*	*K*
hk088	10.9	10.2	24.65	...	23.42	0.41	0.33	0.13	*s*	*K*
hj106[g]	−6.5	12.2	21.79	0.09	...	...	1.06	0.24	*l*	*J*
hj070	−15.4	2.0	22.47	0.17	22.78	...	0.35	0.24	*s*	*J*
hj101[g]	−12.5	11.8	22.70	0.28	...	...	0.60	0.21	*s*	*J*
hj116	14.6	13.0	22.75	0.19	23.29	...	1.88	0.86	*l*	*J*
hj112	8.0	13.0	22.97	0.19	23.38	...	1.05	0.43	*l*	*J*
hj117	13.8	10.8	23.05	0.20	23.23	...	0.96	0.64	*l*	*J*
hj008	−7.3	−22.7	23.19	0.29	22.75	...	0.42	0.37	*s*	*J*
hj114	14.1	13.3	23.37	0.28	23.49	...	0.31	0.27	*s*	*J*
hj118	12.6	12.3	23.38	0.25	23.53	...	0.68	0.32	*s*	*J*
hj102	−2.8	12.2	23.39	0.23	23.46	...	0.91	0.53	*l*	*J*
hj034	−2.8	−14.7	23.48	0.25	23.22	...	0.43	0.31	*s*	*J*
hj030	−4.5	−16.5	23.58	0.22	23.54	...	0.52	0.24	*s*	*J*
hj084	23.8	6.3	23.65	0.33	23.25	...	0.33	0.31	*s*	*J*
hj073	3.5	0.7	23.66	0.19	23.59	...	0.50	0.44	*s*	*J*
hj087	2.8	6.7	23.66	0.20	23.59	...	0.44	0.31	*s*	*J*
hj121	−6.2	14.9	23.76	0.37	23.40	...	0.39	0.41	*s*	*J*
hj065	16.0	−0.5	23.85	0.23	23.55	...	0.34	0.36	*s*	*J*
hj057	−6.8	−3.0	23.85	0.28	23.58	...	0.41	0.18	*s*	*J*
hj054	6.2	−5.0	23.90	0.24	23.59	...	0.37	0.12	*s*	*J*
hj092	22.2	6.8	23.94	0.33	23.41	...	0.33	0.35	*s*	*J*
hj062	23.7	−1.2	23.98	0.39	23.28	...	0.64	0.30	*s*	*J*
hj049	18.9	−6.0	24.01	0.27	23.54	...	0.56	0.20	*s*	*J*
hj109	23.0	12.5	24.03	0.50	23.26	...	0.51	0.21	*s*	*J*
hj089	2.8	8.0	24.07	0.29	23.59	...	0.38	0.40	*s*	*J*
hj025	14.8	−17.8	24.10	0.33	23.47	...	0.50	0.17	*s*	*J*
hj020	20.2	−19.7	24.11	0.43	23.30	...	0.56	0.32	*s*	*J*
hj043	0.2	−10.3	24.13	0.29	23.59	...	0.42	0.28	*s*	*J*
hj018	−−2.1	−19.8	24.17	0.42	23.32	...	0.37	0.25	*s*	*J*
hj055	19.5	−4.6	24.17	0.32	23.53	...	0.58	0.50	*s*	*J*
hj044	22.9	−9.6	24.18	0.37	23.36	...	0.47	0.24	*s*	*J*
hj051	−6.8	−6.3	24.22	0.37	23.58	...	0.40	0.42	*s*	*J*
hj033	11.5	−14.9	24.39	0.37	23.57	...	0.52	0.37	*s*	*J*
hj078	8.9	2.2	24.43	0.36	23.59	...	0.22	0.10	*s*	*J*

TABLE 2—*Continued*

ID (1)	Δx (2)	Δy (3)	J (4)	$\sigma(J)$ (5)	K (6)	$\sigma(K)$ (7)	$\theta_{0.5}$ (8)	$\sigma(\theta)$ (9)	C (10)	S (11)
hj091.....	14.6	7.8	24.44	0.39	23.58	...	0.48	0.53	*s*	*J*
hj095.....	11.9	9.7	24.45	0.41	23.59	...	0.35	0.23	*s*	*J*

NOTES.—Col. (1): Identification label. Col. (2): offset, in arcsec in the x dimension of the NIRC detector. Col. (3): offset, in arcsec, in the y dimension of the NIRC detector. Col. (4): J total magnitude. Col. (5): estimated 1 σ uncertainty in J. Col. (6): K total magnitude, as described in text. Col. (7): estimated 1 σ uncertainty in K. Col. (8): apparent radius for $\eta = 0.5$ [SA 57 radii for sources detected only in the J-band image are scaled by a factor of 0.762 to the seeing conditions of the K-band image based on simulations of model light profiles (see text)]. Col. (9): estimated 1 σ uncertainty in $\theta_{0.5}$. Col. (10): object class, identifying the size of the source, large (*l*) and small (*s*). Col. (11): sample, identifying on which image(s) a source was detected, J and/or K.

[a] Magnitudes listed *without* estimated uncertainties are 1 σ upper limits. Sources missing one of their J- or K-magnitudes were detected in one band but were not within the area of the image for the other band. A few sources have magnitudes and uncertainties listed for both bands, but are too faint, given their location in the images, to be counted in one of the two bands.

[b] Absolute coordinates (epoch 1950) can be generated from Δx, Δy and the rotation of the NIRC detector and coordinates (see Fig. 1):

α[SA576575] = $13^h05^m25^s.80 + (0.0701 \times \Delta x)$ s $-(0.0309 \times \Delta y)$ s ;

δ[SA576575] = $+29°33'44''.3 + (0.404 \times \Delta x)'' + (0.915 \times \Delta y)''$;

α[Herc $-$ 15677] = $17^h19^m43^s.1 + (0.0705 \times \Delta x)$ s $+ (0.0756 \times \Delta y)$ s ;

δ[Herc $-$ 15677] = $+49°49'47'' + (0.731 \times \Delta x)'' - (0.682 \times \Delta y)''$.

[c] sk144 is object SA 57-6575.

[d] hk066 is object Herc 1-5677.

[e] sk201 and hk124 are on the edge of their respective J-band images; J-magnitudes are estimates based on simple aperture photometry.

[f] sk045 and hk076 have size upper limits only.

[g] hj106 and hj101 are sources split from brighter objects in the J-band image with no corresponding sources split in the K-band image. The neighboring brighter source for hj106 is hk099, and for hj101 the brighter, neighboring source is hk091.

depth between fields depends on image class because of changes in seeing; seeing is worse in Herc 1 for the K-band and worse in SA 57 for the J-band. Also note the *large* ($\sim$0.5 mag) difference between the 50% detection limits as a function of image size for a given field and band. Stellar sources have 50% detection limits $\sim$0.5 mag fainter than either of our two categories, *s* and *l*, defined below. *Because completeness falls rapidly with magnitude, accounting for such differences is essential to provide reliable corrected source counts near the detection limits.*

5. PHOTOMETRY, SIZES AND COUNTS

Final photometry consists of 1.″8–2.″1 diameter, fixed-aperture magnitudes corrected to "total" on the basis of object size. The choice of aperture varied from image to image, according to the seeing, in order to make the aperture corrections at most -0.35 mag (as determined empirically from brighter sources in each image and by photometering artificial objects of known size, shape, and brightness that were added into the real images). Object size is defined by the η-function (Petrosian 1976), using the convention of Kron (1995), where η is the ratio of the surface brightness at radius θ to the average surface brightness interior to θ. Sizes were measured from logarithmically spaced, multiaperture photometry for values of $\eta = 0.5$ and 0.1 using the algorithm described in Wirth & Bershady (1998). Such sizes depend only on the surface-brightness distribution and not on amplitude and hence are metric radii.[7] The uncertainty in the measured apparent sizes θ_η is about 50%–75% at the detection limit for $\eta = 0.5$, and somewhat worse for $\eta = 0.1$ (in general $\theta_{0.5} < \theta_{0.1}$). "Total" magnitudes are defined as the light enclosed within the $\eta = 0.1$ radius. With zero points set from stellar sources using the same magnitude scheme (see, e.g., Bershady et al. 1994), and in the absence of noise, these total magnitudes are within $+0.00$, $+0.02$ and $+0.10$ mag of the true total value for Gaussian, exponential, and $r^{1/4}$-law profiles, respectively. Respectively, $\theta_{0.1}$ radii are equivalent to 2.28, 2.86, and 4.39 times these profiles' half-light radii.

For the purpose of counting, we have defined two bins in apparent size $\theta_{0.5}$, adjusted to give the same true apparent size (in the absence of image blur) on each image. Adjustments were made on the basis of simulations of exponential profiles (at various inclinations) and $r^{1/4}$-law profiles (with a range of ellipticities), which all yielded very similar changes in $\theta_{0.5}$ as a function of seeing and intrinsic half-light radius. The specific size (θ_η) that divides the two image classes (small, *s*, and large, *l*) are: $\theta_{0.5} = 0.''62$, $0.''81$, and $0.''71$, respectively, for SA 57 K and J and Herc 1 (J and K). The simulations indicated that the *intrinsic* size is $\theta_{0.5} \sim 0.''44$, i.e., in the absence of image blur. This size corresponds to 3.75 kpc at $z = 1$, or exponential disk scale lengths of 2.1 h_{50}^{-1} kpc ($h_{50} = H_0/50$ km s^{-1} Mpc^{-1}, $q_0 = 0.5$). For Gaussian, exponential, and $r^{1/4}$-law profiles, $\theta_{0.5}$ radii are equivalent to 1.35, 1.07, and 0.17, respectively, times these profiles' half-light radii (1.6 σ for a Gaussian profile, 1.8 scale lengths for an exponential profile).

The raw and corrected counts are listed in Table 1 for each field, band, and image size. Corrections take into account completeness, reliability, and the usable area as a function of depth in 0.5 mag intervals. (The images are of nonuniform depth because of dithering; the Appendix describes how the counts are constructed using the full area.) The values in Table 1 have been averaged over 1 mag intervals but are listed every 0.5 mag, and hence adjacent bins are correlated. Errors include counting statistics (Gehrels 1986) added in quadrature to estimated uncertainties in the completeness corrections based on the variance in the simulations for the set of templates for each

[7] A "metric" radius is defined to mean a measure of size corresponding to the same physical scale for galaxies of the same physical size and light distribution.

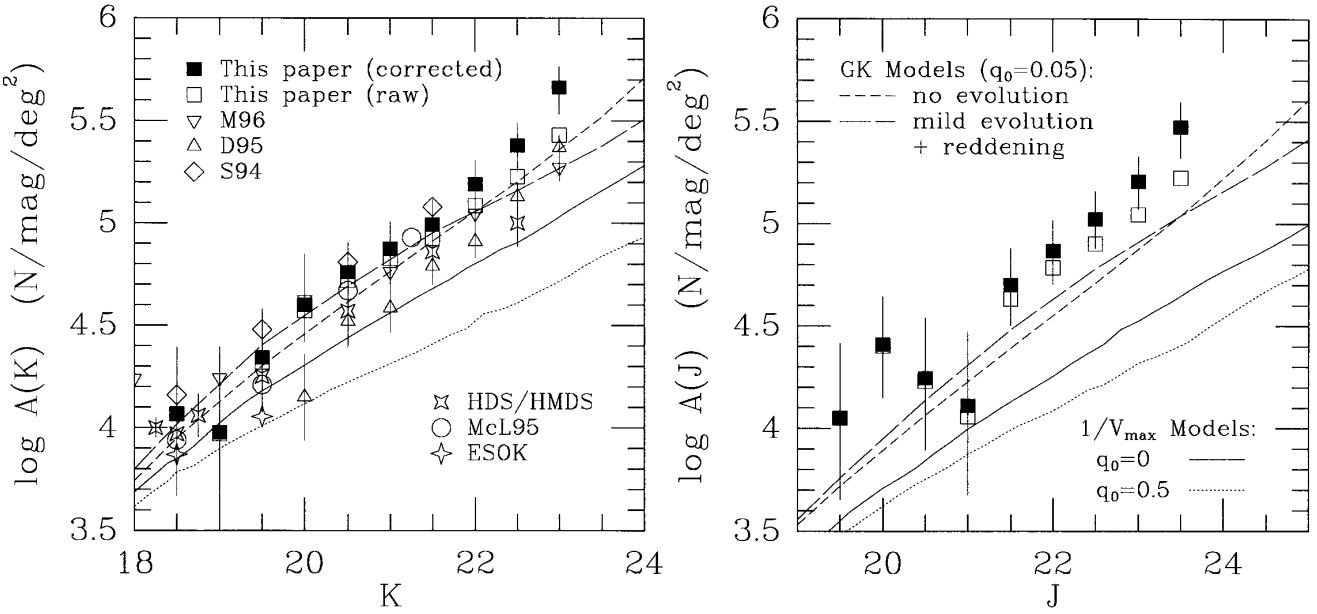

FIG. 4.—Differential counts (number mag^{-1} deg^{-2}) in the K-band (*left panel*) and J-band (*right panel*) for all image sizes combined and averaged over our two fields. Filled squares are corrected for completeness and reliability; open squares are uncorrected. These are compared to other K-band surveys (Moustakas et al. 1997 [labeled "M96"] Djorgovski et al. 1995 ["D95"], Soifer et al. 1994 ["S94"], Gardner et al. 1993 ["HDS/HMDS"], McLeod et al. 1995 ["McL95"], and Saracco et al. 1997 ["ESOK"]); the models of Gronwall & Koo (1995) for $q_0 = 0.05$ (the long-dashed line represents their best-fitting mild evolution model including reddening, and the short-dashed line represents their best-fitting no-evolution model); and our $1/V_{max}$ models for $q_0 = 0$ (*solid line*) and 0.5 (*dotted line*) with no evolution (see text). The Saracco et al. counts ("ESOK") represent the combined data for their two fields ("ESOKS1" and "ESOKS2").

object class (typically $\sim 5\%$). *The counts for each band in a given field are entirely independent.* The total numbers of sources represented in Table 1 are 163 for the K-band and 118 for the J-band. This sample size is somewhat greater than for other near-infrared surveys of similar depth, e.g., 111 and 88 sources to $K24$ by Djorgovski et al. (1995) and Hogg et al. (1997), respectively.

A catalog of JK magnitudes, sizes, and positions for the individual sources used to produce the counts in Table 1 are listed in Table 2. This table also includes several bright sources in bins brighter than those listed in Table 1. Sources are sorted by K-magnitude (or J-magnitude, if detected in only J) separately for each field. For sources detected in only one band, upper limits are tabulated for the other band where possible. Such sources are identified by the absence of photometric error estimates, as described in the table notes. Other details of the data set are noted therein, including astrometric formulae for transforming the relative (x, y) pixel locations into right ascension and declination. We estimate that the relative and absolute astrometry is accurate to $\sim 0\farcs3$ or better.

While Table 2 identifies sources as either small (*s*) or large (*l*), note that we have not distinguished stars from galaxies for the following reasons: (1) there is no clear stellar locus in size-magnitude diagrams, compared to, e.g., those of Kron (1980, his Fig. 9); (2) on the basis of simulations, we found that FOCAS correctly classified stars and galaxies only 50% of the time by $K = 22.5$ for our deepest field; and (3) the apparent lack of stars may be real. Other studies at high Galactic latitudes find 10% contamination at $K = 19.5$–20, consistent with models that predict the fractions of stars to drop to 2% at $K = 21.5$ (Cowie et al. 1994; McLeod et al. 1995). Any stars will be small (*s*) objects in our sample. Most of our detected *s* sources are redder than $J-K \sim 1.25$, which is redder than cool giant and main-sequence stars. Eight are bluer than this value but are coincident in color and magnitude with some *l* sources. While there remains the possibility that we have detected some extremely faint red Galactic stars, it is more likely that these are compact galaxies. Two-color photometry is one way to resolve this issue in the future.

6. J- AND K-BAND GALAXY COUNTS

6.1. *Discrepancies between Surveys?*

What can we infer about faint galaxies from their sizes, colors, and number? We begin by comparing our counts, summed over sizes and averaged over fields, to counts from other surveys as well as from models (see Fig. 4). The last magnitude interval in which all image sizes have detection completeness above 50% in our survey is $K = 23$ (SA 57 only) and $J = 23.5$ (both fields). In order not to introduce an artificial jump in the last K magnitude bin because of field-to-field variations between SA 57 and Herc 1, we have plotted the SA 57 counts in the faintest bin scaled according to their ratio to the average counts, averaged over the previous two bins. For most other surveys no changes have been made to their photometry since their schemes are either comparable to ours or insufficiently specified to attempt adjustment.[8] However, for objects fainter than $K = 21$, Djorgovski et al. (1995) employed aperture corrections that assumed a stellar curve of growth. We find that this assumption results in underestimating the true flux of galaxies and overestimating the depth of their survey by 0.5

[8] A recent paper by Hogg et al. (1997) contains galaxy photometry to $K < 24$ but provides insufficient data to estimate counts. In particular, while they state that their detection is 90% complete to $K = 23$, we estimate based on raw counts constructed from their tabulated source list that there is substantial incompleteness beyond $K = 22.5$ over their full survey area. For this reason, we have not considered their otherwise fine data for counts of galaxies.

mag. Therefore we have applied magnitude corrections to their faint counts to make them consistent with the average aperture corrections we have applied to our data.

Our counts are consistently higher than those of Cowie et al. (1994) and Djorgovski et al. (1995) but are bracketed in amplitude and slope by those of Soifer et al. (1994) and McLeod et al. (1995). (The McLeod et al. survey includes two fields within $\sim 20'$ of our SA 57 field and one field within $9'$ of our Herc 1 field.) While our counts agree roughly with the results of Moustakas et al. (1997) for $K < 21$, our counts are in excess of their counts at fainter magnitudes (a regime where our data are significantly more complete). Since the Soifer et al. (1994) and McLeod et al. (1995) samples end at $K \sim 21.5$, our counts represent a substantial increase in the number of measured galaxies at $K \geq 21.5$. The slope of our K counts ($d \log [A(K)]/dm = 0.36 \pm 0.02$)[9] is slightly shallower than that of Djorgovski et al. (1995), as plotted in Figure 4. Had we not made the large ~ 0.5 mag corrections to the counts of Djorgovski et al. (1995), we would then have comparable slopes but more discrepant amplitudes. With the exception of Moustakas et al. (1997), who report a slope of ~ 0.23, counts from all other surveys are substantially steeper than the value of 0.26 reported by Gardner et al. (1993), which was based on data from Cowie et al. (1994). Indeed, both this survey and that of Djorgovski et al. (1995) yield count slopes that do *not* decrease for $K > 21.5$ but show some hint of an increase, in contrast to the Gardner et al. and Cowie et al. results. Our J-band counts also show no sign of a flattening slope at the faint end and reach surface densities equivalent to our values at $K \sim 22.7$ but are well in excess of values from other faint K surveys at this depth. The J counts have a comparable slope to our K-band counts ($d \log [A(J)]/dm = 0.35 \pm 0.04$). There are no J data in the literature for an independent direct comparison.

To what extent are the variations in counts and slopes due to large-scale structure? Within our own data, field-to-field variations in the counts are within the Poisson counting noise for a given magnitude bin but do vary systematically with magnitude. Herc 1 is 20% higher than SA 57 for $19.5 \leq K \leq 20.5$, while SA 57 is 30% higher than Herc 1 for $21 \leq K < 22.5$. A similar trend occurs in the J counts, with Herc 1 having a higher surface-density at brighter magnitudes ($21 \leq J \leq 22$). Slopes for the individual fields are 0.35 ± 0.02, 0.27 ± 0.05 for $19.5 < K < 22.5$ and 0.46 ± 0.04, 0.34 ± 0.06 for $20.5 < J < 23.5$ for SA 57 and Herc 1, respectively. These K-band slopes are within—but span—the bounds observed by others.

Is either of our fields representative? We have addressed this question using a cell-count analysis of the deep $KG3$-($\sim R$-) band catalog covering 30.2 arcmin^2 from the drift-scan survey of Hall & Mackay (1984). We find that our SA 57 field is low relative to the average cell of its size by about $30\% \pm 17\%$ over the magnitude range $20 < KG3 < 25$ but becomes more representative at the faintest magnitudes, yet it is still low by $15\% \pm 10\%$. Surface densities at $KG3 = 25$ are comparable to what we find at $J \sim 21.5$ and $K \sim 20.5$. For Herc 1, we have checked against a photographic catalog to $R_F = 23$ covering 0.384 deg^2 (Munn et al. 1997) to find that for $21 < R_F < 23$, Herc 1 has a $30\% \pm 34\%$ surfeit of galaxies. The surface density of objects to $R_F = 23$ (Kron 1980) is comparable to the surface density at $K = 19$. While these checks are rather uncertain, they are consistent with Herc 1 being somewhat unrepresentatively high at the bright end of our near-infrared counts. We have, however, no independent optical check at this time for the faint end of our near-infrared counts.

Given the small size and great depths of these fields, it is plausible that large-scale structure is producing variations in the counts as a function of magnitude. Over all magnitudes, the field-to-field variations within our sample are at a $\sim 30\%$ level, two-thirds of which is expected from Poisson noise. The remainder is only slightly higher than the $\sim 10\%$ variation expected from clustering in images of this size and depth estimated by Djorgovski et al. (1995). The consistently lower counts of Djorgovski et al. (1995) and Cowie et al. (1994) are also plausibly caused by real variations in the counts. Larger, ultradeep surveys are needed to resolve this issue.

6.2. *A Comparison to Models*

6.2.1. *The Models of Gronwall & Koo*

It is instructive to compare the current data to models, two sets of which are shown in Figure 4. The models of Gronwall & Koo (1995) predict that the counts do *not* roll over at $K \sim 22$ and may in fact steepen beyond $K = 23$, much like our data. These models include both passive evolution and the effects of internal extinction due to dust, both of which are included in the derivation of luminosity functions. The luminosity functions are constrained to fit observational data of faint galaxies. These data include counts and distributions in color and redshift for a wide range of surveys, but they do not include the K-band counts from our work, Djorgovski et al. (1995), or Moustakas et al. (1997). Our counts are in excess of those predicted by the Gronwall & Koo model for $K > 21.5$ and for all magnitudes in the J-band that are well constrained by these data ($21.5 < J < 23.5$). The excess reaches about a factor of 2 for $K = 23$ and a factor of 2.7 for $J = 23.5$. For $\log A \sim 5.2$ mag^{-1} deg^{-2}, the excess is $\sim 40\%$ in K and a factor of 2 in J. This occurs at $K = 22$ and $J = 23$, implying a mean galaxy color contributing to this excess of $J - K = 1$. This is about 0.5 mag bluer than the median color at these magnitudes, but objects with these colors are plentiful in our sample, as we will show. Figure 5 shows that based on $J - K$ color, such galaxies would lie at very low redshifts ($0.05 < z < 0.25$) if there is no color evolution. Alternatively, these galaxies could have a much wider range of possible redshifts if they are undergoing a very strong burst of star formation seen very early on in the burst (also illustrated in Fig. 5). Hence, the usual ambiguity between strong evolution in color and luminosity and a nonevolving, steep, faint-end luminosity function applies to the interpretation of these data (see, e.g., Koo & Kron 1992).

6.2.2. $1/V_{\rm max}$ *Empirical Simulations*

The second set of models, labeled $1/V_{\rm max}$, are empirical simulations. They are based on a U- though K-band observational survey of low-redshift galaxies (Bershady et al. 1994), which has been scaled, object by object, by the relative accessible volumes in the input survey and the output simulations. Hence galaxy evolution does not enter into these models, and the only free parameters are those that specify the curvature (q_0 and Λ_0; we assume $\Lambda_0 = 0$ here). Because the input survey has U- through K-band photo-

[9] Slope uncertainties quoted throughout are 67% confidence intervals for one free parameter.

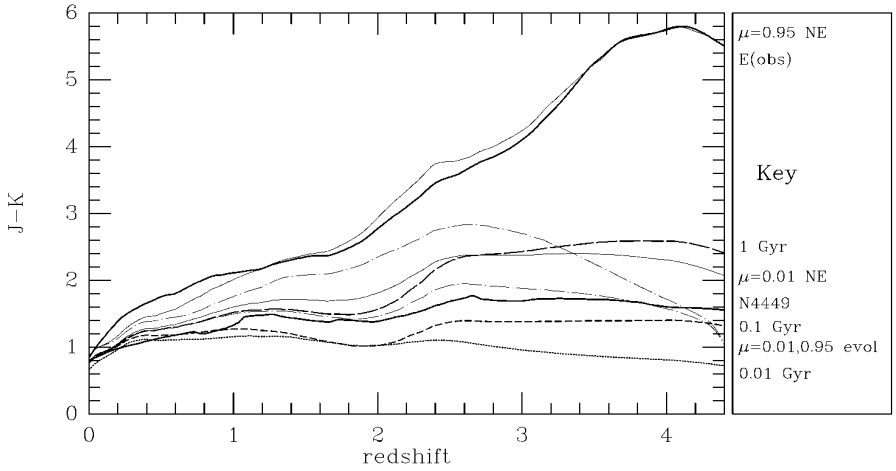

FIG. 5.—Synthetic $J-K$ color vs. redshift for model and observed SEDs (Bruzual & Charlot 1993). (1) Unevolving colors for an observed elliptical and NGC 4449 (*heavy solid lines*) and 16.4 Gyr models for $\mu = 0.01$ and 0.95 (*light solid lines*), where μ is the fraction of galactic mass converted to stars each Gyr. $H_0 = 50$ km s^{-1} Mpc^{-1} and $q_0 = 0$ is assumed throughout. (2) Evolving colors for 16.4 Gyr models ($z_{\rm formation} \sim 5$) and for $\mu = 0.01$ and 0.95 (*dot-dashed lines*). (3) Colors for constant age 0.01 Gyr (*dotted lines*), 0.1 Gyr (*short-dashed lines*), and 1 Gyr age for a $\mu = 0.95$ model as they would be observed at each redshift. Note that only the unevolving SEDs corresponding to today's ellipticals rise above $J-K = 3$. For reference, the color of a flat f_ν spectrum is $J-K = 0.97$.

metry, k-corrections in the K-band are determined empirically for each simulated object[10] (Bershady 1995). As a result, the effects of internal extinction due to dust are empirically accounted for; this is not a model parameter. However, the input sample, while it extends 7.5 mag fainter than M_K^* (0.001 L_K^*), contains few galaxies (16) fainter than $M_K^* + 5$ (0.01 L_K^*) because it is a relatively small, magnitude-limited sample (roughly $B < 20.5$ and 0.9 deg^2). Hence estimates of the contribution from dwarf galaxies remain somewhat uncertain. $1/V_{\rm max}$ models substantially underpredict our observed counts by $K = 20$ but stay within a factor of 2 until $K > 22$ for $q_0 = 0$.

6.2.3. *The Contribution of Low-Luminosity Galaxies to the Counts*

Can the models' underprediction of the observed counts plausibly be explained by low-luminosity galaxies, e.g., missing in the $1/V_{\rm max}$ input sample? Low-luminosity galaxies are expected to be present in significant numbers by $K \sim 20$, but the precise contribution depends on the currently unknown faint end of the local K-band luminosity function. Remarkably, a 0.01 L_K^* galaxy can be seen to $z \sim 0.8$ at $K = 23$, but at this distance only 3%–10% of the survey-limited volume is included. This estimate depends on q_0 and assumes a redshift upper limit of $z = 4$, where $K = 23$ corresponds to L_K^*. Nonetheless, galaxies in our $1/V_{\rm max}$ models with $0.001 < (L/L^*)_K < 0.01$ contribute roughly 30% and 60% of the counts at $K = 23$ for $q_0 = 0$ and 0.5, respectively.

Lower luminosity galaxies, however, are expected to contribute insignificantly to the faint counts. The slope of the K-band luminosity function for the $1/V_{\rm max}$ models' input survey (Bershady et al. 1998) is well described by $\alpha = -1.6$ for $M_K < -23$ ($\sim$0.06 L_K^*, $H_0 = 50$, $q_0 = 0$). Using this slope to extrapolate the observed space densities fainter than 0.001 L_K^*, we find that galaxies with $0.0001 < (L/L^*)_K < 0.001$ would contribute only 5% and 12% of the counts at $K = 23$ for $q_0 = 0$ and 0.5, respectively. Therefore, the largest uncertainties in the predicted $1/V_{\rm max}$ model counts at the depths probed in our study here come from the luminosity function in the range $0.001 < (L/L^*)_K < 0.01$, *unless* there is a very strong upturn at even fainter luminosities in the already steep observed slope of the luminosity function.

Consider, for example, how much the faint-end luminosity function slope must be steepened in the range 0.001–0.01L^* to fit the counts at $K = 23$ with little or no evolution. Referring to Figure 4, this requires a $\sim$15 times increase in the integrated volume density of such galaxies for the $1/V_{\rm max}$ models ($q_0 = 0$ and 0.5), and between a factor of 6.5 and 8.5 increase for the models of Gronwall & Koo (no evolution and mild evolution, $q_0 = 0.05$). This corresponds roughly to changing the faint-end slope α (as parametrized by the Schecter function) by $\Delta\alpha \sim -0.4$ over the same modest luminosity range for the $1/V_{\rm max}$ models, and less over larger ranges of luminosity. For the models of Gronwall & Koo, $\Delta\alpha \sim -0.3$ would suffice. Such steeper slopes cannot be ruled out, since recent results from local surveys yield values of α discrepant by at least this amount (e.g., compare results from Marzke et al. 1994 with those of Loveday et al. 1992 or Lin et al. 1996). The volume density of such low-luminosity galaxies is thus not well constrained at any redshift. Certainly $\Delta\alpha \sim -0.3$ would be possible within the uncertainties of the luminosity function determined from our $B < 20.5$ sample or from the deeper surveys of Lilly et al. (1995) and Ellis et al. (1996). With such uncertainties, the amount of evolution needed to fit the counts remains unknown. If $q_0 = 0.5$, either substantially more evolution or an even steeper luminosity function is needed than in the low-q_0 case. We emphasize that this conclusion is based not on the slope of the counts, but rather on their amplitude.

6.2.4. *Cosmological Interpretation of the Count Slope and Amplitude*

The $1/V_{\rm max}$ models and those of Gronwall & Koo (1995) allow us to explore the sensitivity of the counts to luminosity function parameters and, in turn, whether the counts can be used reliably to probe q_0. While the $1/V_{\rm max}$ models substantially underpredict our observed counts, they only

[10] This is true for $z = 7$, which is not exceeded in our simulations.

moderately underpredict the count slope for $K > 20$. For $q_0 = 0$, they yield close to the same slope as the models of Gronwall & Koo (1995). In the J-band, the $1/V_{max}$ models predict even fewer galaxies than either the data or the models of Gronwall & Koo (1995), but again the slopes are comparable. Unlike other no-evolution models (see, e.g., Fukugita et al. 1990, as used by Gardner et al. 1993; or Yoshii & Takahara 1988, as used by Cowie et al. 1990 and Djorgovski et al. 1995), for $q_0 = 0.5$, our $1/V_{max}$ model predicts that the counts do *not* roll over around $K = 22$, but instead continue to rise beyond $K = 25$ and $J = 25$. This reflects a steeper faint-end slope of the local K-band luminosity function than previously adopted by model builders. Yoshii & Takahara (1988) and Fukugita et al. (1990) both adopt $\alpha = -1.11$, whereas our value is closer to -1.6. Similarly, Gronwall & Koo (1995) derived a faint-end slope of the luminosity function that was somewhat steeper than that of Metcalfe et al. (1991) for the bluest galaxies but otherwise was quite comparable to that of Marzke et al. (1994). The luminosity function for the latest galaxy types (which dominate the cumulative luminosity function at low luminosity) from Marzke et al. (1994) is described by $\alpha = -1.87 \pm 0.2$.

Why then do counts predicted from recent *observational* determinations of the K-band luminosity function also roll over around $K = 22$ for $q_0 = 0.5$ (Mobasher, Sharples, & Ellis 1993; Glazebrook et al. 1995; Gardner et al. 1997)? None of these surveys contain low-luminosity galaxies in sufficient number to constrain the faint-end slope. For example, Mobasher et al. use no data fainter than $M_K \sim -23$ (only $\sim 0.1L^*$) to derive their luminosity function, while Glazebrook et al. simply adopt $\alpha = -1$. It is relevant to note that these two surveys derive different M_K^* and ϕ^* (by roughly a factor of 2 for each parameter, but in the opposite sense) such that the bright end of the predicted counts match the observations. Counts at bright magnitudes are little affected by the value of α. For example, the effective M_K^* and ϕ^* of our local sample also fit the bright end of the counts ($K < 17$), as illustrated in Figure 6, even though our value of α is considerably more negative. In contrast, M^* and ϕ^* little affect the slope of the faint end of the counts, and only ϕ^* affects the count normalization.

In general, for steep luminosity functions, the slope of the counts becomes increasingly dependent on α at fainter magnitudes. As a consequence of the steep faint-end slope of the luminosity function of our local sample (Bershady et al.

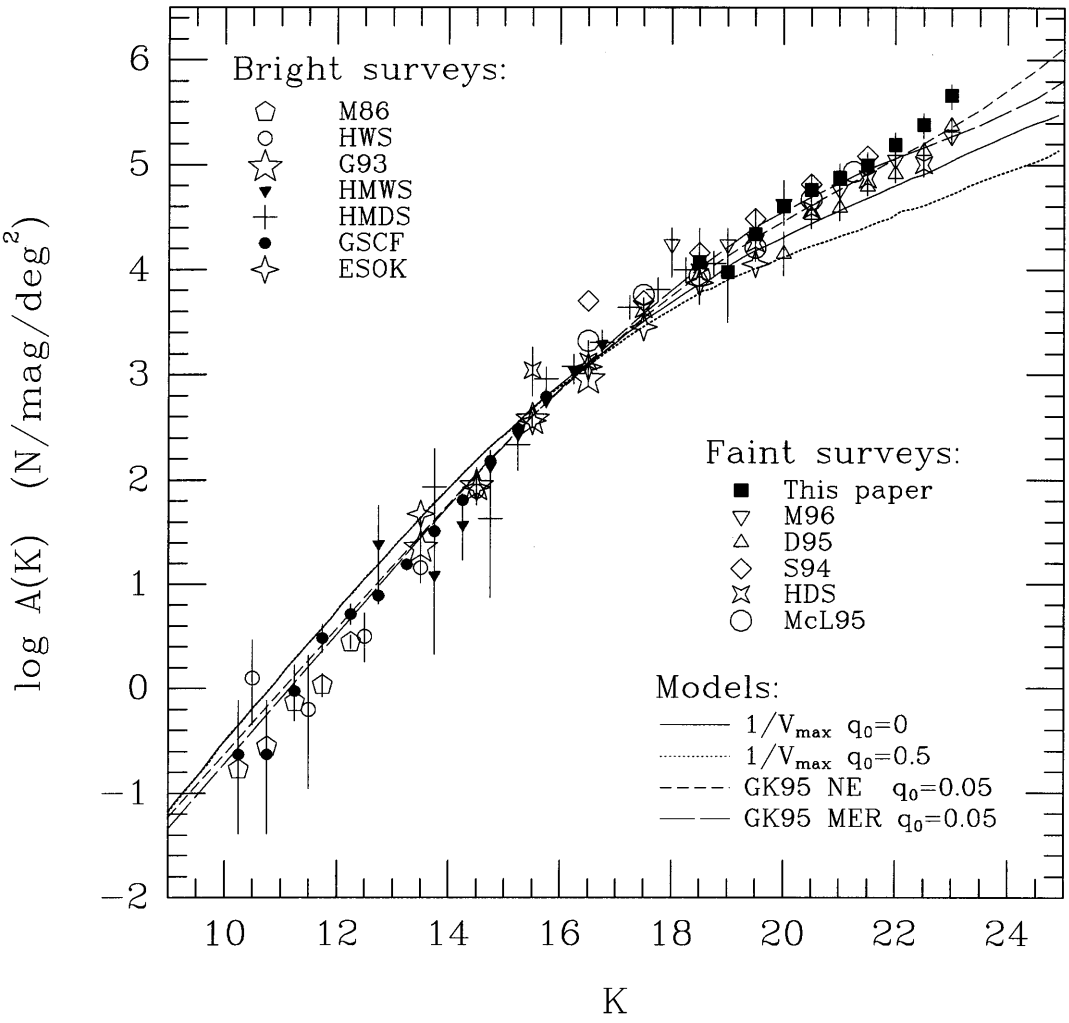

FIG. 6.—Differential counts (number mag^{-1} deg^{-2}) in the K-band for all published surveys, including this survey. M96, D95, S94, HDS/HMDS, McL95, and ESOK surveys are defined in the legend to Fig. 4. Other surveys include Mobasher et al. (1986; labeled "M86"), Gardner et al. (1993; "HWS/G93"), and Gardner et al. (1996; "GSCF"). Models are the same as in Fig. 4.

1998), the model counts at faint magnitudes are increasingly dominated by low-L galaxies at relatively low redshifts. This in turn makes the slope of the faint end of the K-band counts insensitive to q_0 as well as to the cosmological constant. However, Figures 4 and 6 do show that the count amplitudes differ significantly (by a factor of ~ 2 at $K = 23$) between $q_0 = 0$ and 0.5. *For a steep luminosity function slope, it is the amplitude of the counts that is most affected by cosmological parameters.*

Djorgovski et al. (1995) comment, however, on their inability to use even the amplitude of the faint K counts to constrain geometry because of its sensitivity to many model parameters, including evolution. This sensitivity is well illustrated in the simple models presented by Koo (1990). Our analysis with the $1/V_{\rm max}$ models and with those of Gronwall & Koo (1995) in the previous section indicates that the slope of the faint end of the luminosity function is critical in determining not only the count slope but the count amplitude as well. Hence, even ignoring the effects of evolution, there is no aspect of the faint counts (slope or normalization, either in the optical or near-infrared–infrared) that can be used reliably as a cosmological probe without firm knowledge of the faint end of the galaxy luminosity function and its evolution.

7. SIZE, COLOR, AND EVOLUTION OF FIELD GALAXIES

7.1. *The Excess Revealed: Counts as a Function of Image Size*

We can place additional constraints on galaxy evolution and cosmology by exploiting our size information. In particular, galaxy size can be used to estimate luminosity in special circumstances. Recall that there is less than a 20% change in apparent size for $0.8 < z < 3.5$ and $0.1 < q_0 < 0.5$. To $K = 23$, our $1/V_{\rm max}$ model predicts that $\sim 75\%$ of the galaxies will be at such redshifts or higher, and this fraction is only weakly dependent on q_0. Locally, galaxy luminosity is observed to be tightly correlated with size. If this is not a surface-brightness selection effect in local samples, and in the absence of size or luminosity evolution, then apparent size should continue at large redshifts to correlate strongly with luminosity. Properly calibrated, size could be used to estimate luminosity in this regime (modulo cosmological assumptions). Hence the relative excess and slopes of small (s) and large (l) galaxies may yield clues to the nature of the excess for the entire sample.

We start this analysis by taking advantage of the $1/V_{\rm max}$ models, which transform various information, including sizes, from the input sample into the output simulations. Full accounts of the PSFs are included. More specifically, each object's size and shape (i.e., image concentration) is compared to a grid of models appropriately smoothed to derive the transformation. These transformations are expected to be accurate and free of substantial bias because (1) the input radii are large enough that the transformations depend weakly on object shape and vary slowly with object size; (2) the input sample, taken in 0.″8–1.″2 seeing (FWHM) and at a median redshift of 0.13, is typically better resolved than the output sample; and (3) we have an accurate estimate of both input and output PSFs.

Figure 7 compares the expected size distribution from the model (for $q_0 = 0$ only) to that of the data, in the form of differential counts for small (s) and large (l) objects. The shaded areas indicate the variations in the observed counts if the size delimiter between s and l is varied by $\pm 10\%$ (spanning 30% of the dynamic range in size), and they show that the qualitative behavior of the counts is not sensitive to such variations. Our $1/V_{\rm max}$ model predictions of the M_K and z distributions to $K = 23$ are tabulated in Table 3 for $q_0 = 0$. In the absence of strong evolution, large (l) galaxies should correspond to L^* galaxies observed at $z \sim 2$, while small (s) galaxies correspond to sub-L^* galaxies typically at

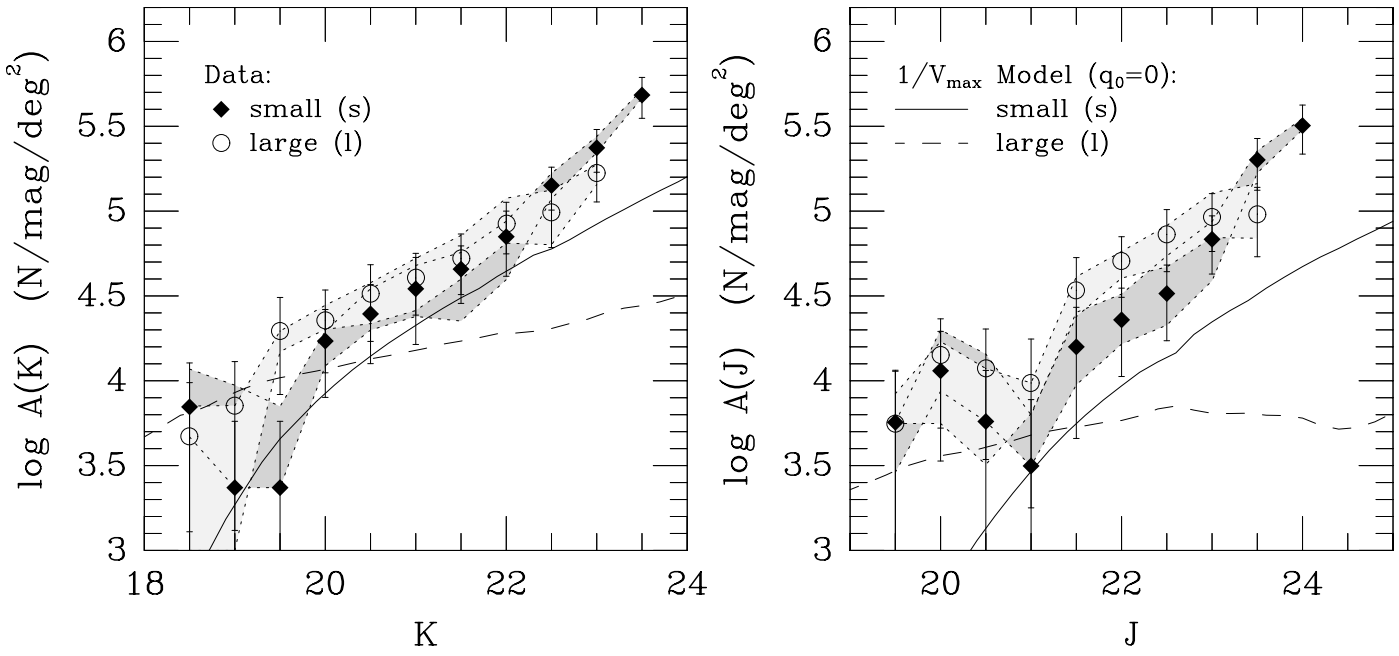

FIG. 7.—Differential counts (number mag^{-1} deg^{-2}) in the K- and J-bands for small (s) and large (l) galaxies, averaged over both fields. These are compared to our $1/V_{\rm max}$ model simulations with no evolution for $q_0 = 0$. Image sizes and model are defined in § 6.2. Shaded areas indicate changes to the counts when the size delimiter between small (s) and large (l) is varied by $\pm 10\%$ (*dark shaded area* for s; *light shaded area* for l).

TABLE 3

$1/V_{max}$ NO-EVOLUTION MODEL PREDICTIONS FOR $q_0 = 0$

	CUMULATIVE DISTRIBUTIONS TO $K \leq 23$						MEDIAN $(J-K)$ AS A FUNCTION OF K				
	M_K			z							
CLASS	25%	50%	75%	25%	50%	75%	17.5–18.5	18.5–19.5	19.5–20.5	20.5–21.5	21.5–22.5
All.....	−24.9	−23.9	−22.2	0.80	1.46	2.06	1.78	1.99	2.25	2.36	2.40
s.....	−24.0	−23.1	−20.9	0.64	1.25	1.80	1.55	1.82	1.93	2.06	1.99
l.....	−25.8	−25.2	−24.3	1.16	1.84	2.44	1.79	2.07	2.44	2.52	3.37

NOTE.—For reference $M_K^* = -25.1$ ($H_0 = 50$ km s^{-1} Mpc^{-1}).

$z \sim 1$. According to our findings in § 5, if these galaxies are mostly disk-dominated systems, large galaxies should have half-light radii ($r_{1/2}$) in excess of 3.5 h_{50}^{-1} kpc, while small galaxies will have $r_{1/2} < 3.5\, h_{50}^{-1}$ kpc.

The observed slope for the *s* counts is in good agreement with the model until $K = 22$ and $J = 22.5$. Recall that we expect the estimate of the *s* counts to be too low because of the limited local sample for the $1/V_{max}$ model input (i.e., the $1/V_{max}$ model underrepresents the true number of low-luminosity objects even in the absence of evolution). The relative increase in the excess for *s* counts between *J* and *K* can plausibly be explained by color-luminosity effects and redshift effects, both of which work in the same direction to make the apparent colors of lower luminosity objects bluer. The observed crossover point at $K \sim 22$ and $J \sim 23$ illustrates again why the counts do not roll over. According to the $1/V_{max}$ simulations, low-luminosity objects dominate the counts at the faintest magnitudes and are observed at relatively low redshifts where the differential volume is still increasing rapidly with luminosity distance.

The surprising result is that the count excess is greatest for larger (*l*) galaxies. This relative excess increases slightly in *J*. The observed crossover (where *s* and *l* surface densities are equal) is about 1.7 mag fainter than the model predictions, while the color at the crossover is as predicted ($J-K \sim 1$). Qualitatively, the model difference in the slopes of the *s* and *l* counts matches that seen in the data; however, the model amplitude for *l* counts is very low while the observed slope is relatively steeper.

7.1.1. *Comparison to Optical Observations*

We can check our results against two other recent studies that have probed the size distribution of galaxies to comparable depth at optical wavelengths. Smail et al. (1995) find a median half-light radius that has an asymptotic value of 0.″2 at $R \sim 26$, based on ground-based images from Keck in comparable seeing to our near-infrared data. This limit is comparable to $K = 23$–23.5, about 0.75–1.25 mag fainter than our crossover point where our median intrinsic $\theta_{0.5} =$ 0.″44. For the most favorable case (Gaussian profile), $\theta_{0.5}$ would correspond to a half-light radius of 0.″33. At $R \sim 25$, Figure 4 of Smail et al. indicates their half-light radius is approaching 0.″3, and hence their results and ours are in close agreement.

An independent comparison can be made from the results of Roche et al. (1996), who have measured sizes in the *I*-band from deep WFPC2 images. Roche et al. measure a median half-light radius of 0.″18–0.″2 in the range $25 < I < 26$. This is comparable to Smail et al.'s depth, if we adopt their median $R-I$ of 0.35 at $R = 26$. In the range $23.5 < I < 24.5$, which corresponds closely to $K = 22$ (cf. Figs. 8 and 9 of Moustakas et al. 1997), Roche et al. measure a median half-light radius of 0.″25–0.″32. Hence their results agree with both the results of Smail et al. and our own. Together, these three studies indicate the size distribution of galaxies at these depths are comparable when measured at wavelengths between 0.65 and 2.2 μm. As a consequence, the excess of apparently large, faint galaxies observed in our deep near-infrared images should be found in deep optical images as well.

7.2. *Constraints from Near-Infrared Colors*

In addition to the amplitude and slope of the counts with and without size information, colors can place constraints on the nature of the excess galaxy population in these deep near-infrared images. The usefulness of the single $J-K$ color available for our sample as a redshift indicator is limited for field galaxies of diverse intrinsic colors, although it has been attempted (Ellis & Allen 1983). Figure 5 shows that synthetic $J-K$ colors for a range of observed and model spectral energy distributions (SEDs) span a considerable range in observed color at a given redshift. In particular, colors as blue as $J-K \sim 1.5$ are consistent with any redshift above 1, based solely on observed SEDs. The redshift discrimination is worse if galaxy light is dominated by stellar populations of very young ages. However, $J-K$ does offer significant leverage for discriminating redshifts of galaxies with intrinsically red colors.

Figure 8*a* shows the $J-K$, *K* color-magnitude diagram for galaxies in our sample within the deepest portion of either the *J* or *K* images (i.e., within 0.5 mag of full depth). While it excludes part of the sample used for counting, this subsample should be representative. Figure 8*a* also extends to fainter magnitudes than the counts. The total area sampled is $\sim 0.3 \times 10^{-3}$ deg^2, and the total number of objects is 241. The median colors to $K = 22.5$ for the *s* and *l* samples are listed separately and combined in Table 4. The medians include objects with upper limits but are always bluer than the bluest of these upper limits. Note the presence of a large number of galaxies fainter than $K = 21.5$ with colors near $J-K = 1$ and the absence of many objects

TABLE 4

OBSERVED MEDIAN $(J-K)$ AS A FUNCTION OF K

Class	17.5–18.5	18.5–19.5	19.5–20.5	20.5–21.5	21.5–22.5
All.....	1.73	...	1.38	1.57	1.54
s.....	1.69	...	1.38	1.75	1.64
l.....	1.85	...	1.66	1.43	1.49

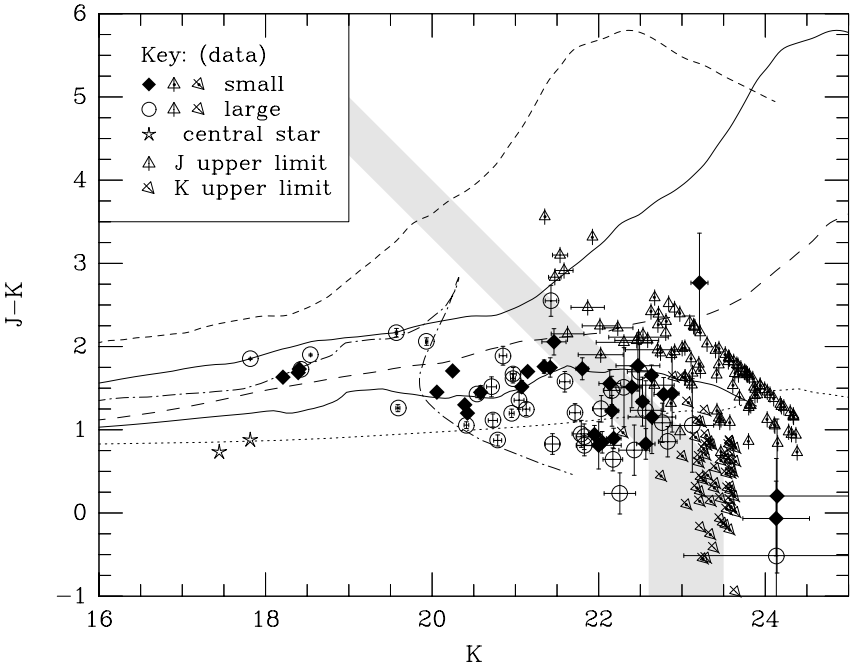

FIG. 8*a*

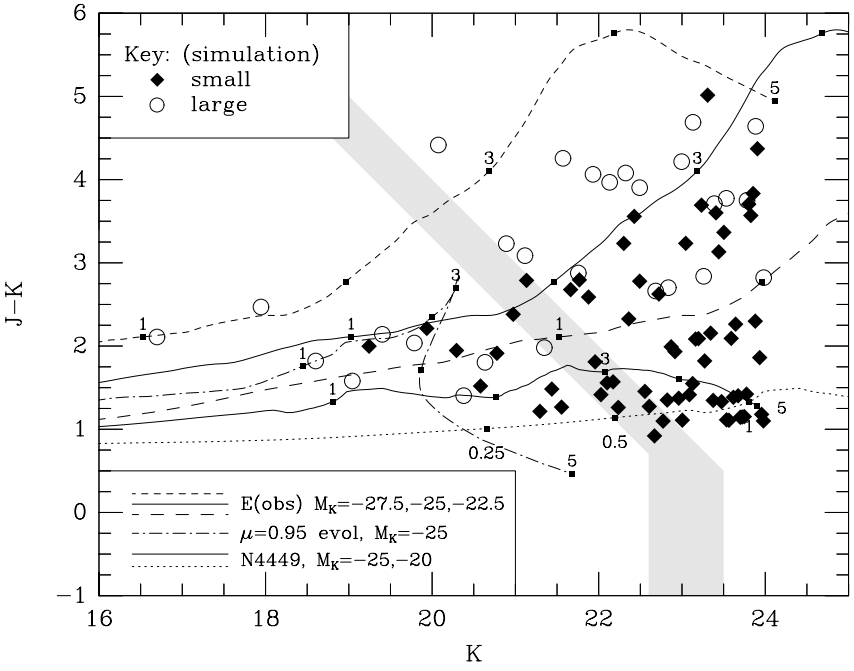

FIG. 8*b*

FIG. 8.—(*a*) $J-K$ vs. K for objects observed in the deepest portion (to within 0.5 mag of full depth) of either the J or K images (both fields). Objects are marked as coded in the key. Objects detected in only one band have their other magnitude and color calculated with 2 σ upper limits and are included to depths (in their detected band) 0.5 mag fainter than the 50% detection limit for stellar sources. The shaded area represents the 50% detection limits in J and K for the *s*- and *l*-type objects in both fields. Error bars are marked for all objects detected in both J and K and for all drop-outs brighter than $K = 22.5$. Model redshift tracks are labeled and described in (*b*). (*b*) $J-K$ versus K Monte Carlo simulation for $q_0 = 0$ based on our $1/V_{max}$ empirical models for the same area as the observed sample in (*a*). Objects are marked as coded in the key, with the determination of "large" and "small" based on the same criterion as the observed sample (see text). Shaded areas representing the 50% detection limits of the observed sample are repeated here. The simulation, however, is limited strictly to $K < 24$. Model redshift tracks are shown for an observed (nonevolving) elliptical galaxy SED near M_K^* (*top solid line*; $M_K = -25$, $H_0 = 50$, $q_0 = 0$); the same galaxy spectrum, 10 times brighter (*short-dashed line*; $M_K = -27.5$), and 10 times fainter (*long-dashed line*; $M_K = -22.5$); a blue star-forming galaxy near M_K^* (*bottom solid line*; N4449, $M_K = -25$); the same galaxy spectrum, 100 times fainter (*dotted line*; $M_K = -20$); an evolving $\mu = 0.95$ model with a present day age of 16.4 Gyr and $M_K = -25$ (*dot-dashed line*; Bruzual & Charlot 1993). Redshifts of 1, 2, 3, 4, and 5 are marked with small squares and labeled for $z = 1, 3$ for $M_K \leq -22.5$ tracks; redshifts of 0.25, 0.5, and 1 are marked and labeled for the $M_K = -20$ track.

redder than $J-K = 2$. Qualitatively, this behavior is similar to the $I-K$ versus K color-magnitude diagrams of Hogg et al. (1997) for $20 < K < 22.5$. We have used their data to quantitatively check that, for all galaxies combined, their trends in median $I-K$ with K are similar to our trends in median $J-K$ with K.

For comparison, Figure 8*b* illustrates one Monte Carlo simulation of the expected color-magnitude distribution

based on our nonevolving $1/V_{max}$ models for $q_0 = 0$. This simulation matches the effective observed area as a function of depth. However, the simulation does not include the observed detection completeness but, instead, is strictly limited to $K < 24$. (Note that the median model values listed in Table 3 use much larger simulations.) In both figures, redshift tracks for several fiducial galaxy spectra and luminosities are plotted; these are discussed below.

The observed median $J-K$ color for small (*s*) galaxies is 1.6 mag, with *no trend* in magnitude. While the lack of a trend is consistent with the model prediction, the observed median color is about 0.3 mag bluer than the model prediction (Table 3). If more lower luminosity galaxies were included in the model input sample, the resulting redshifts would become lower and the colors bluer. Hence it is quite plausible that the *s* galaxy population is consistent with little to no evolution in an open universe.

On the other hand, the median $J-K$ color for large (*l*) galaxies is 1.6 mag averaged to $K = 22.5$ but gets progressively bluer at a rate of 0.1 mag per mag. By $K = 22.5$, the observed median *l* galaxy color is over 1 mag bluer than the model predictions and has the opposite trend of color with magnitude. The observed median *l* galaxy color is also slightly bluer (~ 0.15 mag) than the median *s* galaxy color fainter than $K = 20.5$, also in disagreement with the models. In the models, the reddening trend for the *l* galaxies is caused by luminous, unevolved, early-type galaxies seen at progressively larger redshift with increasing depth (refer also to Fig. 5). The blueing trend is in no way anticipated by the nonevolving $1/V_{max}$ models.

7.3. *Evolution*

7.3.1. *What Are the Excess Large, Near-Infrared Blue Galaxies?*

We offer three explanations for the difference between observations and the $1/V_{max}$ models, two of which are plausible, and a third, which, while compelling for other reasons, we can rule out. First there is the possibility of evolution, either in luminosity, color, or both. There is now ample evidence, e.g., from the Canada France Redshift Survey (Lilly et al. 1995), that between $z = 1$ and $z = 0$ there has been modest luminosity evolution for blue galaxies, with possibly a steepening of the blue galaxy luminosity function, while there is little change in the luminosity function for the redder galaxies. The form of this evolution is qualitatively in the correct sense to explain the increased number of blue galaxies. For example, $J-K$ for blue, star-forming galaxies at $z = 1$ is ~ 1.5. However, this solution would require also an evolution in size (decreasing with time), as might occur in a scenario in which galaxies at higher redshifts are observed in the process of merging. In addition, there should be almost no very red galaxies at high redshift: while an L^* galaxy should be detectable to $z \sim 4$ at $K = 23$, there are few galaxies observed with $J-K > 2$, while the median *l* model galaxy color at $K = 22$ is 3.4. As we discuss further below, this indicates that we are probing a redshift regime where ellipticals are observed at very young ages.

Another possibility is that our sample is revealing a high space density of low surface brightness dwarfs, detected here at relatively low redshift ($z < 1$). Holmberg (1975) pointed out that lower luminosity galaxies tend to have lower surface brightness. This trend is seen in our input sample for the $1/V_{max}$ models. What is required to fit the deep K observations is a substantially larger dynamic range in surface brightness for a given luminosity than currently observed, along the lines of what has been suggested by Ferguson & McGaugh (1995) and plausibly demonstrated by McGaugh, Bothun, & Schombert (1995). This situation would violate one of the conditions for apparent size and luminosity to be well correlated. Likewise, if galaxies are detected at sufficiently low redshift, apparent size and luminosity are expected not to correlate.

This second scenario can be presented as two extreme possibilities: for low surface brightness dwarfs to dominate the *l* counts, they will need to be at (1) $z < 0.8$ for $L < 0.01L^*$ or (2) $z < 0.07$ for $L < 0.0001L^*$. The former case (1) cannot be ruled out by our data, and moreover it is difficult to distinguish between this scenario and one in which high-redshift, luminous, young galaxies contribute to the excess large blue galaxy population. The primary reason for this is that their observed blue colors at disparate redshifts are quite comparable, both in the optical and the near-infrared. This is illustrated in Figure 8*b* for $J-K$, where two spectra for N4449 are shown assuming a factor of 100 (5 mag) difference in luminosity. The two redshift tracks in this figure differ in $J-K$ color by ~ 0.5 mag at a given apparent K-magnitude; between redshifts of 0.5 and 2, $J-K$ changes by ~ 0.2 mag. Recall also that if sufficiently young galaxies are present at any redshift, $J-K$ offers almost no leverage for estimating redshift (Fig. 5). The near degeneracy in color and redshift are still worse in the optical, as illustrated in Figure 9.

For case 2, galaxies must be very red in the optical to produce a median color of $J-K = 1.6$ at such low redshifts. Such an abundant population of faint red galaxies has yet

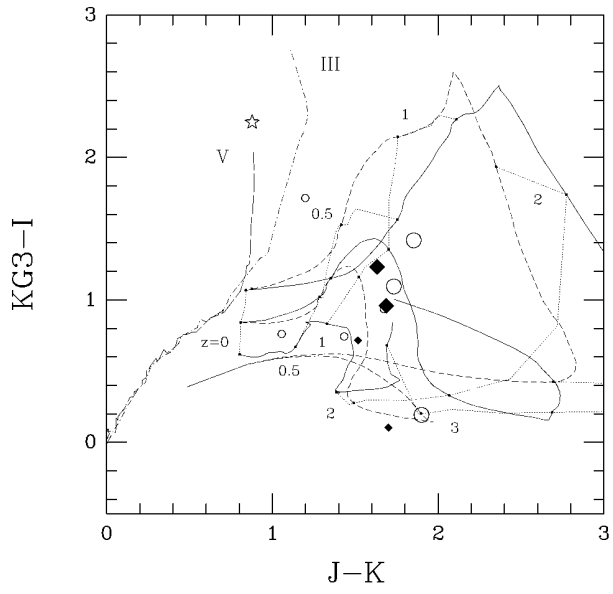

FIG. 9.—$KG3 - I$ vs. $J-K$ for 12 objects matched in the deepest region of our SA 57 field to the catalogs of Hall & Mackay (1994). *KG3* is similar to but broader than *R*. Symbols are coded as in Figs. 7 and 8, with larger symbols for $K < 19$ and smaller for $20 < K < 21.5$. The stellar loci for main-sequence and giant stars are shown as long- and dot-dashed lines, respectively. Redshift tracks for nonevolving galaxies (*solid lines*, top to bottom) are for an observed elliptical, the $\mu = 0.1$ model, and N4449. Redshift tracks for passively evolving galaxies (*short-dashed lines*, top to bottom) are for $\mu = 0.95$ and 0.1. Models are described in the legend to Fig. 4. Redshifts are indicated at 0, 0.5, 1, 2, and 3, and connected between different SEDs by dotted lines.

to be directly confirmed at low to intermediate redshift, but they have long been suggested to exist as the "end state" of post–star-forming galaxies (see, e.g., Searle, Sargent, & Bagnuolo 1973; Huchra 1977; Babul & Rees 1992). If true, this would be the first evidence for their existence. At a limiting redshift of 0.07, there is only about 2 h_{50}^{-3} Mpc^3 down to $K = 22.5$ accessible in our survey. Hence if such objects dominate the counts at this depth for large galaxies, their space density is of order 30 h_{50}^{-3} Mpc^{-3}.

We can test this low-redshift, red dwarf galaxy scenario (case 2) by checking the optical colors of our sample, taking advantage of the $KG3$- and I-band data in one of our fields from Hall & Mackay (1984). While their catalogs are not as deep as ours, we have matched 14 objects, only two of which are not in the deep portion of the near-infrared images (both happen to be very red in $J-K$). Of the remaining 12, plotted in Figure 9, six are brighter than $K = 19$. Of these, one is the central star with characteristically red $R-I$ and blue $J-K$. Four of the others are consistent with intermediate galaxy spectral types between $1 < z < 1.5$ ($0.9 < R-I < 1.2$), while the sixth is very blue ($R-I = 0.2$) and consistent with $2.5 < z < 3.5$ for a blue galaxy spectral type. The remaining six are between $20 < K < 21.5$ and are of the most interest since they are faint enough to sample the region where there is a significant excess of large, blue galaxies. Two of these are s galaxies, with colors consistent with blue galaxy spectral types between $1 < z < 3$. Of the four l galaxies, two are consistent with blue-to-intermediate galaxy spectral types between $1 < z < 3$. The third is very red in $R-I$ given its $J-K$ color and falls between the elliptical track and the stellar locus. The fourth is consistent with blue spectral type around $z = 0.25$. In summary, there is *no evidence* for any galaxies at $z < 0.25$ to $K = 21.5$, and only one galaxy plausibly at $z < 1$ with red optical colors. The majority (seven of 11) of galaxies have colors consistent with blue to intermediate spectral types at $1 < z < 1.5$. Moustakas et al. also find that most of their faint galaxies have blue $V-I$ colors. Hence, we can rule out the possibility that there exists a high space density of red dwarf galaxies at low redshift in the field.

7.3.2. *Optical Confirmation of an Excess of Large, Optically Blue Galaxies*

Roche et al. (1996) also find an excess of galaxies with large half-light radii ($>0\farcs4$) with blue optical colors ($V-I < 1.2$) in the range $22 < I < 24$. This excess is claimed with respect to their own no-evolution and pure luminosity evolution models, which use a steep luminosity function slope comparable to ours ($\alpha = -1.65$). The excess large galaxies, they note, appear morphologically to be spirals and irregulars, but not ellipticals. It is reasonable to assume that Roche et al. are indeed observing the optical counterpart of the excess population of large, near-infrared blue galaxies in our survey. Does this information offer new clues as to the nature of these galaxies?

Their interpretation is that this excess of large galaxies is caused by a 1 mag brightening of today's L^* galaxies by $z = 1$–2. However, they also find a large number of small objects in the same magnitude range and with similar colors (the distribution peaks at $V-I \sim 0.8$ for both). They interpret the small galaxies as dwarfs at $z < 0.5$, present because of their steep luminosity function slope. To support this distinction between small and large galaxies with the same optical colors, they marshal evidence from spectroscopic surveys (see, e.g., Lilly et al. 1995) that indicate 1 mag of luminosity evolution for bluer galaxies by $z = 1$, and the "chain" galaxies of Cowie, Hu, & Songaila (1995) at $22 < I < 23$, which are large, blue, and in the range $1 < z < 1.6$. On the other hand, recent spectroscopic results from Koo et al. (1996) identify the bulk of the galaxy population to $I < 24$ as sub-L^* with a median redshift of ~ 0.8. Neither the depths nor the completeness of the faintest spectroscopic surveys is sufficient to determine quantitatively the contributions from low and high redshifts to the large blue galaxy population observed at $I \sim 26$ or $K \sim 23$.

An alternative scenario to pure luminosity evolution is the bursting dwarf hypothesis of Babul & Ferguson (1996). Roche et al. (1996) dismiss this model because they claim the predicted size distribution is too small. However, close scrutiny of Babul & Ferguson's Figure 18 shows that the predicted size distribution to $I \sim 25$ is not unreasonable, with a peak in the half-light radius distribution near $0\farcs25$. What is more problematic for Babul & Ferguson's model is the $I-K$ versus K color-magnitude diagram, which shows far too few blue galaxies by $K = 22$ compared to, e.g., Figure 8 of Moustakas et al. (1997). Moreover, bursting dwarfs are not needed to keep the K counts rising, and indeed a steep nonevolving luminosity function can match the same observations, as we have demonstrated. The most important test of the bursting dwarf hypothesis will be to see if the K counts for small objects rise more steeply for $K > 23.5$ than illustrated in Figure 7 for $K < 23.5$.

Finally, it is worth commenting on the results of the infall formation models calculated by Cáyon, Silk, & Charlot (1996), which predict that smaller half-light radii should accompany luminosity evolution. If one accepts the luminosity evolution scenario favored by Roche et al. (1996), one would expect that there would not be an excess of large, blue galaxies at faint magnitudes. Roche et al. (1996) dismiss the alternative possibility that there exists a substantial population of low surface brightness dwarfs in their sample. They claim selection effects would keep such objects out of their sample. However, at a given *apparent* size and surface brightness, there is no preference for photometrically detecting a galaxy at low or high redshift. Perhaps, then, there is further reason to consider the possibility that relatively low-redshift, low surface brightness dwarfs contribute substantially to the large, blue galaxy excess population. The question remains, therefore, how low surface brightness dwarfs at relatively low redshifts ($z \sim 0.5$) can be distinguished from high surface brightness giants at high redshift ($z > 1$) when both have similar, extremely blue colors yet are beyond the limits of spectroscopy. This question cannot be answered here with the current data.

7.3.3. *A Deficit of Red Galaxies?*

While we have focused our attention on interpreting the nature of the surfeit blue galaxies, particularly those with large image sizes, it is relevant to consider whether the $1/V_{\rm max}$ models predict too many red galaxies. An observed absence of red galaxies might indicate that at least one source of the blue excess population are early-type galaxies observed at high redshift, when they were more luminous and bluer in color. Because we can use $J-K$ instead of an optical or optical-infrared color, we are much less sensitive to recent but small (in terms of mass) bursts of star formation superimposed on old, underlying stellar populations. In this sense, $J-K$ puts stronger limits on the presence or

absence of galaxies whose light is dominated by old stellar populations (cf. Zepf 1997).

To $z \sim 3$, the nonevolving $1/V_{\max}$ model $J-K$ colors are comparable to passively evolving models of present-day ellipticals with formation redshifts (z_f) greater than ~ 10 (see Fig. 5 from McCarthy 1993). Luminosity evolution, however, which is *not* included in the $1/V_{\max}$ models, *is* appreciable for passively evolving models even in the near-infrared. Luminosity evolution in the K-band amounts to ~ 0.5 mag at $z = 1$ and ~ 1 mag at $z = 2$ in an open universe for passively evolving models of present-day ellipticals with $z_f > 4$. This means that we can set strong upper limits on the number of red objects expected for passive evolution, since sources will only brighten but not become bluer with redshift. Hence the predicted number of red sources within our survey limit will only increase in the passively evolving scenario with respect to no-evolution models.

Operationally, we define a "red envelope" in the $J-K$ versus K color-magnitude diagram (Figs. 8*a* and 8*b*) as that region redward or brighter than the redshift track for an unevolving elliptical with absolute magnitude near L_K^*. It is important to keep in mind that, because there is no direct redshift information, at any given apparent magnitude and color there is an ambiguous trade-off between luminosity and redshift for a given SED. The ambiguity increases when other SEDs are included. For this reason, we restrict the analysis to luminosities above L_K^* corresponding to the reddest SEDs, since galaxies with bluer SEDs are expected to be preferentially at lower luminosities (in the absence of evolution). However, in order to check the sensitivity of our threshold, we also define a second, more inclusive envelope using the redshift track for the same red SED with absolute magnitude near $0.1\ L_K^*$.

Note that in the absence of evolution, some very luminous ($L_K > 10\ L_K^*$) galaxies are expected in deep samples. The simulated objects in Figure 8*b* at the reddest colors for a given magnitude are not intrinsically "ultra"-red, but simply overluminous. At great depths one might expect even more luminous objects to be found: while such objects are rare, more volume is sampled than in the input sample of our $1/V_{\max}$ models. For example, Hu & Ridgeway (1994) found two "red" objects at $I = 18.5$ ($I-K = 6.5$), which they believe, based on *BIJHK* colors, are unevolved ellipticals at $z = 2.4$ and $10L^*$. However, Graham & Dey (1996) find one of these objects appears to have broad emission consistent with Hα at $z = 1.44$. If true, this is indicative of intensive star formation or nuclear activity, and the red colors indicate dust and not an old population. Nonetheless, the upper envelope used by Elston, Rieke, & Rieke (1988) in $R-K$ versus K (corresponding to $M_V = -23.3$, $H_0 = 50$, $q_0 = 0$), for example, would have excluded two galaxies at moderate redshifts with luminosities 0.4 mag brighter than but with the colors of present day ellipticals from Bershady (1995). In the spirit of placing an upper limit on the number of galaxies with old stellar populations, no upper limit in luminosity or color is imposed on our selection of red-envelope galaxies.

The numbers of objects observed and predicted from the $1/V_{\max}$ models to lie above the L_K^* and $0.1\ L_K^*$ red envelopes are presented in Table 5 in three intervals of K-magnitude. For $q_0 = 0$, the number of observed $> L_K^*$ galaxies is very close to predictions for small galaxies, whereas the observed number is too low by about a factor of 3 for large galaxies. The number of observed $> 0.1\ L_K^*$ galaxies is low by about 30% for both large and small galaxies. However these deficits are only a 1–2 σ result, given the small total number of objects. If the J-band upper limits are all assumed to lie above the adopted envelopes, there are no deficits in the last magnitude bin ($21.5 < K < 23$). Excluding these upper limits, the expected number of large $> L_K^*$ galaxies is higher than observed at all magnitudes, while for $> 0.1\ L_K^*$, the deficit is only in the two fainter bins.

For $q_0 = 0.5$, the expected number in the same region of color and magnitude is roughly the same for large (*l*) galaxies (which are predominantly intrinsically red in the models), but much lower for small galaxies (which are predominantly intrinsically blue in the models). The reason for this is that, to first order, the smaller volume to a given redshift in a critical universe is offset by the smaller luminosity distance. Hence, at a given apparent magnitude and redshift, one sees fainter in the luminosity function. For bluer galaxies, however, the k-corrections are more favorable, and one sees galaxies of comparable rest frame luminosity at higher redshifts where there is less volume. Hence

TABLE 5

OBSERVED AND $1/V_{\max}$ NO-EVOLUTION MODEL DISTRIBUTIONS IN $J-K$ VERSUS K

		$K < 20$			$20 < K < 21.5$			$21.5 < K < 23$		
CLASS	SAMPLE	$> L_K^*$	$> 0.1\ L_K^*$	$< 0.1\ L_K^*$	$> L_K^*$	$> 0.1\ L_K^*$	$< 0.1\ L_K^*$	$> L_K^*$	$> 0.1\ L_K^*$	$< 0.1\ L_K^*$
All.....	Observed	0	8	1	2	3	22	3 (29)	13 (29)	48 (32)
	$1/V_{\max}\ q_0 = 0$	2	7	1	6	8	5	6	18	12
	$1/V_{\max}\ q_0 = 0.5$	4	5	1	4	6	2	3	5	10
s.....	Observed	0	3	0	1	1	10	1 (17)	6 (17)	28 (17)
	$1/V_{\max}\ q_0 = 0$	0	2	0	2	3	4	1	9	12
	$1/V_{\max}\ q_0 = 0.5$	0	0	1	0	2	2	0	0	10
l.....	Observed	0	5	1	1	2	12	2 (12)	7 (12)	20 (15)
	$1/V_{\max}\ q_0 = 0$	2	4	1	4	5	1	5	9	0
	$1/V_{\max}\ q_0 = 0.5$	4	5	0	4	4	0	3	5	0

NOTES.—Counts in bins of $J-K$ and K are divided according to the redshift tracks in Fig. 8. "$> L^*$" includes objects above the upper solid line; "$> 0.1L^*$" includes objects above the long-dashed line; "$< 0.1L^*$" includes objects below the long dashed line. The sum of "$> 0.1L^*$" and "$< 0.1L^*$" give the total number of objects in each K-magnitude bin. Numbers in parentheses for the faintest bin are the observed counts if all 2 σ J-band upper limits are assumed to be above the solid and long-dashed lines. The $1/V_{\max}$ model counts for $q_0 = 0.5$ are referenced to the tracks in Fig. 8, which are calculated for $q_0 = 0$. For both $q_0 = 0$ and 0.5, the model counts are mean estimates using large simulations scaled to the appropriate observed area. These means are rounded to the nearest integer and have uncertainties consistent with counting statistics.

in a critical universe, bluer galaxies are diminished in number relative to redder galaxies at a given apparent magnitude.

A tentative result is that our observations are inconsistent at the $\sim 1.5\ \sigma$ level with the expected number of old, luminous ($L > L^*$) galaxies in the range of $1 < z < 3$. This result is insensitive to cosmological assumptions.

Given our low number statistics, it is more fruitful to ask if the observed deficit of red, luminous galaxies could be responsible for the surfeit of blue galaxies, large and small. For example, the redshift track of an evolving model galaxy with the present day colors of an elliptical but with $z_f = 5$ is shown in Figures 8*a* and 8*b*. This illustrates one possible way that a red-envelope galaxy would evolve and become bluer with apparent magnitude (redshift). From Table 5 we estimate that only as much as 10%–30% of the large, blue galaxy excess, and 20%–30% of the small blue galaxy excess, can be made up in this way in the range $20 < K < 23$. The percentage declines toward fainter magnitudes. The remaining excess must therefore come from some as yet indeterminate combination of galaxies evolving to $\sim L^*$ and blue colors, and a steep luminosity function, as we have previously discussed.

7.3.4. *Evolution Away from the Red Envelope*

What other evidence is there that early-type galaxies have substantially evolved at $z > 1$? From other deep imaging surveys, for example, Djorgovski et al. (1995) show an absence of objects with red $r - K$ for $K > 21.5$. At somewhat brighter limits, Cowie et al. (1994, 1995) also show an absence of objects with red $I-K$ for $K > 20.5$. Cowie et al. (1994) note that the surface density of faint, red ($I-K > 4$) galaxies is less than what would be expected in the absence of evolution. Their comparison, though, is to the expected surface density for all galaxies integrated to 8 mag fainter than L^* (Gardner et al. 1993).

There is, however, abundant recent evidence that red galaxies in clusters become more luminous in the past. Luminosity evolution has been inferred to $z = 1.2$ using the Tolman test (Dickinson 1995; Pahre, Djorgovski, & de Carvalho 1996; Schade et al. 1996), and to $z = 0.4$ using Fundamental Plane relations (Van Dokkum & Franx 1996; Bender, Bodo, & Bruzual 1996). In these analyses, red galaxies are assumed not to have evolved in size. These studies conclude that changes in luminosity with redshift are consistent with passive evolution in clusters. Lilly et al. (1995) find little evidence for luminosity evolution in the field for red galaxies in the range $0 < z < 1$. Yet the study of Schade et al. (1996) finds evidence for luminosity evolution in both field and cluster ellipticals.

Evidence for color evolution in red galaxies has been less forthcoming. In clusters, however, Aragon-Salamanca et al. (1993) found that by $z = 0.9$ few cluster members were as red in $R-K$ as present day ellipticals. Recent results from Stanford, Eisenhardt, & Dickinson (1998) also show that elliptical galaxy cluster members do appear to get bluer over the range $0 < z < 0.9$, consistent with expectations of passive evolution and large z_f. However, this amounts to $J-K$ getting bluer by less than 0.2 mag for cluster E/S0 galaxies over this redshift range. A more dramatic form of evolution has been claimed by Kauffmann, Charlot, & White (1996). Upon reanalysis of Lilly et al.'s data, they find that two-thirds of the galaxies "earlier" than Sa are gone by $z = 1$, assuming passive luminosity evolution and $z_f = 5$ ($H_0 = 50$, $q_0 = 0.5$). Notably, Lilly et al. (1995) performed a similar analysis and inferred no evolution in color if no evolution in luminosity were assumed (consistent with their own results for the luminosity function of red galaxies).

There is no doubt that *some* galaxies that are red enough to be consistent with old, evolved stellar populations do exist at substantial redshifts. In the field, Koo et al. (1996) find several such sources to $z = 1$ in optically selected samples. A large fraction of Westerbork millijansky sources are optically identified (to $V < 21.5$) as unevolved giant ellipticals up to $z \sim 1$ (Kron, Koo, & Windhorst 1985; Windhorst, Koo, & Spinrad 1986). Recently, one such source has been identified at $z = 1.55$ (Dunlop et al. 1996). However, what is not known from these studies is just what fraction of the expected sources are still consistent with what we have defined as the "red envelope." The McCarthy (1993) summary of the optical counterparts to 3CR and 1 Jy sources indicates that, for $z > 1.5$, $J-K$ colors broaden and become as blue as $J-K = 1.25$. This color is bluer than the median colors in our sample. Some radio sources, however, are as red as our red envelope in $J-K$ at least to $z = 2.5$.

In summary, there is ample evidence for evolution in luminosity and optical-infrared colors in cluster ellipticals up to $z = 1$, but the evidence for field and radio samples is less secure or at least the evolution is less homogeneous. By $z > 1.5$, color evolution manifests itself in the near-infrared ($J-K$) for radio samples. Nonetheless, some red-envelope radio galaxies are still found at higher redshifts. Our results here are broadly consistent with the results from the radio surveys. However, constraints on the formation epochs of early-type galaxies is far from secure from those data. McCarthy (1993) argues, for example, that the $r-K$ and $J-K$ colors of radio galaxies are together inconsistent with a single-burst model for the star-forming history of radio galaxies. Regardless of the actual physical scenario, independent observational evidence indicates that our observation of a deficit of faint red-envelope galaxies (corresponding to early-type galaxies at $z > 1$) is plausible.

8. SUMMARY

Our deep Keck near-infrared images have reached surface densities of $\sim 300{,}000\ \mathrm{mag}^{-1}\ \mathrm{deg}^{-2}$ at $J = 23.5$ (corresponding to $K = 22.75$), which is equivalent to optical counts at depths of $B = 27$ and $I = 26.5$ (Metcalfe et al. 1995; Smail et al. 1995; Williams et al. 1996). Our K-band data go somewhat deeper and reach a surface density of $\sim 500{,}000\ \mathrm{mag}^{-1}\ \mathrm{deg}^{-2}$ at $K = 23$. This surface density is higher than any published ground-based B counts and within 50% of the surface densities for the Hubble Deep Field in V- and I-bands (Williams et al. 1996).

A robust result, not dependent on color or size, is that the K-band counts do not roll over by $K = 22.5$. The same is true for the J-band at comparable surface densities.

The excellent seeing conditions have allowed us to use size and color together to identify the dominant galaxy type contributing to the counts. By the faintest magnitudes, the smallest galaxies (i.e., within the bottom 50% of the size range for galaxies to these depths) begin to dominate the counts and have a median $J-K$ of ~ 1.6. This trend in size and $J-K$ color of the smallest galaxies is qualitatively anticipated from our no-evolution models based on an empirically determined, local field galaxy luminosity function. Such galaxies, according to our models, correspond to relatively low-luminosity ($L < 0.1L^*$) galaxies at $z < 1$;

their abundance is due to a relatively steep faint end slope for the K-band luminosity function, dominated by blue galaxies at low luminosities.

As long as the volume density of galaxies continues to rise at lower luminosities, the counts should continue to rise and be relatively insensitive in slope to the cosmological volume. Even in the absence of evolution (though strong evolution is likely at these depths), improved measures of the faint end of the luminosity function must be obtained before galaxy counts can be used as a cosmological probe.

We have also been able to isolate the dominant galaxy type contributing to the count excess, as reckoned with respect to mild- or no-evolution models. The most striking result of our deep near-infrared survey to $K = 23$ is that there is a substantial excess of apparently large galaxies (i.e., within the top 50% of the size range for galaxies at these depths), compared to models with no evolution. These galaxies are very blue in $J-K$ if they are at intermediate or high redshifts ($z > 0.5$), but relatively red if they are at very low redshifts ($z < 0.25$). Hence this implies (1) a "new" population of low-redshift, low surface-brightness, low-luminosity red galaxies, (2) an intermediate-redshift population of moderately blue, diffuse galaxies with luminosities in the range 0.001–0.1L*, (3) a strongly evolving population of galaxies at high redshift observed at $L \geq L$*, or (4) some combination of the three. We can rule out the first option based on the blue optical ($R-I$) colors of a random subset of our sample. However, weighing the contributions from the second and third options is not possible without spectroscopy or perhaps detailed morphological information provided from higher resolution images.

We also find a relative paucity of very red galaxies compared to models with no evolution. This deficit is in a region of $J-K$ color and K-magnitude corresponding to early-type galaxies brighter than L* at $z > 1$ in the models. If it is assumed that such distant galaxies have evolved to have bluer colors, then they can account for no more than 30% of the excess blue galaxies, large and small. The result is insensitive to the assumed value of q_0. Further study of the absence of these red-envelope galaxies at faint magnitudes should provide constraints on the epoch of early-type galaxy formation.

We would like to thank W. Harrison for excellent support and assistance with the NIRC, G. Wirth for his collaborative effort in investigating new size statistics for faint object work, C. Gronwall for access to her models, S. Majewski for access to CCD data in Herc 1, and P. Hall & C. McKay for access to CCD data and catalogs in SA 57. M. A. B. acknowledges support from NASA grant NAG 5-6032 and faculty research funds from Penn State University and the University of Wisconsin, Madison. M. A. B. and J. D. L. acknowledge support from NASA through grant numbers HF-1028.02-92A and HF-1048.01-93A, respectively, from the Space Telescope Science Institute, which is operated by the Association of Universities for Research in Astronomy, Incorporated, under contract NAS 5-26555. D. C. K. acknowledges support from NSF grant AST-88-58203 and faculty research funds from the University of California, Santa Cruz.

APPENDIX

CONSTRUCTION OF DIFFERENTIAL COUNTS IN IMAGES OF NONUNIFORM DEPTH

The following is a step-by-step calculation of the counts in Table 1 for one case: SA 57, K-band, s-type. In general the entire available area of each final image is used (i.e., Figs. 1 and 2). These images are mosaics of many frames with a range of offsets. Consequently the depth within the image is not uniform and must be accounted for. This is necessarily a complicated calculation.

1. *Raw counts* (N).—The raw counts are first tabulated in 0.5 mag intervals, as listed in Table A1 (cols. [1] and [2]). The magnitudes define the center of the intervals. The counts, when extracted from the catalog for each image, are truncated not at a fixed magnitude but at a fixed S/N such that the faintest counts come only from the deepest (and smallest) area. That is, instead of

$$m < m_{50} ,$$

we specify

$$m - 1.25 \log (t/t_{\max}) < m_{50} ,$$

where t is the average value of the exposure map for pixels within the object aperture and $t_{\max}$ is the maximum value in the image. Hence m_{50} is the magnitude limit (corresponding to 50% detection) in the deepest part of the image.

One further condition is made: in the deepest part of the image, we count 0.5 mag fainter than in the other parts of the image. This is accounted for when calculating the effective area (below in step 3). The point of this is to push the counts as deep as possible at full depth, while not introducing noisier detections at brighter magnitudes from the outskirts of the image.

2. *Completeness function* (df).—This is determined for the deepest part of the image, as listed in Table A1 (col. [3]). The quantity $\Delta(df)$ (col. [4]) is the estimated uncertainty in the measurement of df based on scatter in simulations of detection completeness. The index j (col. [5]) is referred to in (3b) below.

3. *Area* (S).—Here areas are calculated for each depth. This accounts for the fact that the sample is cut at a fixed S/N.

a) We start with an image representing the square root of the exposure map of the data image. The former has units of the square root of the number of frames, $t^{1/2}$, contributing to each pixel in the final data image. The maximum value is $(t_{\max})^{1/2} = 9.35$, i.e., about 88 frames. Then we count the number of pixels down to $t^{1/2} \sim 0.32$, i.e., 1/10 frame, in steps of $t^{1/2}$

TABLE A1

RAW COUNTS AND COMPLETENES

K (1)	N (2)	df (3)	$\Delta(df)$ (4)	j (5)
18.25.....	2	1.000	0.000	1
18.75.....	0	1.000	0.000	2
19.25.....	0	1.000	0.000	3
19.75.....	0	1.000	0.000	4
20.25.....	2	0.964	0.011	5
20.75.....	1	0.959	0.008	6
21.25.....	7	0.951	0.008	7
21.75.....	5	0.934	0.019	8
22.25.....	7	0.898	0.050	9
22.75.....	15	0.810	0.096	10
23.25[a].....	16	0.630	0.140	11
23.75[b].....	21	0.401	0.147	12

NOTES.—Col. (1): K magnitude at center of 0.5 mag interval. Col. (2): Raw counts in 0.5 mag interval. Col. (3): Fractional completeness in deepest portion of image. Col. (4): Estimated uncertainty in df. Col. (5): Running index from brightest to faintest magnitude intervals.

[a] Count limit for 1.25 log $(t/t_{max}) < -0.5$.

[b] Count limit for 1.25 log $(t/t_{max}) \geq -0.5$.

corresponding to 0.5 mag steps in limiting depth. (Less than 1 frame can contribute to a pixel because the frames are registered on a subpixel level.) The lower limit is somewhat arbitrary but unimportant because the area converges. (For example, the number of pixels between $0.01 < t^{1/2} < 0.37$ is 515, or 0.5% of the total area). The pixel counts (N_{pix}) in these intervals are listed in Table A2 (cols. [1]–[3], respectively). The index i (col. [5]) is referred to immediately below. The magnitude difference, dm, between the deepest and the ith interval is listed in column (4).

b) For each magnitude interval m, we sum up the areas in Table A2 starting with the deepest, and ending when $m + dm$ corresponds to the last entry in Table A1 (the completeness file, step 2 above) or the last entry in Table A2, whichever comes first. To account for how we counted in step 1, only the faintest magnitude interval may use the last entry in the completeness file. Hence the total area S_{tot} is

$$S_{tot}[m(j)] = \sum_{i=1}^{\min(i_{max},\, j_{max}-j)} N_{pix}(i)\,, \qquad j < j_{max}$$

and

$$S_{tot}[m(j)] = \sum_{i=1}^{\min(i_{max},\, j_{max}-j+1)} N_{pix}(i)\,, \qquad j = j_{max}\,,$$

where j is the index in column (5) of Table A1, i is the index in column (5) of Table A2; j_{max} and i_{max} are the maximum values (respectively 12 and 7). S_{tot} is listed in column [2] of Table A3 in units of square degrees assuming a plate scale of 0.″1515 pixel^{-1}.

TABLE A2

PIXEL COUNTS

	$t^{1/2}$				
N_{pix} (1)	Maximum (2)	Minimum (3)	dm (4)	i (5)	LEVEL (6)
69261.....	9.35	5.90	0.0	1	Deepest
18575.....	5.90	3.72	0.5	2	
10651.....	3.72	2.35	1.0	3	
4929	2.35	1.48	1.5	4	
11600.....	1.48	0.94	2.0	5	
4493	0.94	0.59	2.5	6	
1361	0.59	0.37	3.0	7	Shallowest
Total = 120870					

NOTES.—Col. (1): Pixel counts in the image representing the square root of the exposure map, $t^{1/2}$, in the interval min $< t^{1/2}t <$ max. Col. (2): Maximum value of $t^{1/2}$ corresponding to a 0.5 mag interval. Col. (3): Minimum value of $t^{1/2}$ corresponding to a 0.5 mag interval. Col. (4): Magnitude difference between deepest and shallowest exposure map intervals. Col. (5): Running index from deepest to shallowest exposure map intervals.

TABLE A3

AREA, EFFECTIVE AREA, AND CORRECTED COUNTS

K (1)	S_{tot} (2)	S_{eff} (3)	Boost (4)	A (5)
18.25.....	0.214E−03	0.213E−03 ± 0.236E−06	1.006 ± 0.001	$0.188E+05^{+0.248E+05}_{-0.121E+05}$
18.75.....	0.214E−03	0.212E−03 ± 0.206E−06	1.008 ± 0.001	$0.000E+00^{+0.000E+00}_{-0.000E+00}$
19.25.....	0.214E−03	0.211E−03 ± 0.335E−06	1.013 ± 0.000	$0.000E+00^{+0.000E+00}_{-0.000E+00}$
19.75.....	0.214E−03	0.209E−03 ± 0.723E−06	1.024 ± 0.004	$0.000E+00^{+0.000E+00}_{-0.000E+00}$
20.25.....	0.214E−03	0.202E−03 ± 0.192E−05	1.058 ± 0.010	$0.198E+05^{+0.261E+05}_{-0.128E+05}$
20.75.....	0.212E−03	0.196E−03 ± 0.255E−05	1.080 ± 0.014	$0.102E+05^{+0.235E+05}_{-0.844E+04}$
21.25.....	0.204E−03	0.184E−03 ± 0.335E−05	1.105 ± 0.020	$0.761E+05^{+0.410E+05}_{-0.281E+05}$
21.75.....	0.183E−03	0.165E−03 ± 0.359E−05	1.111 ± 0.024	$0.606E+05^{+0.410E+05}_{-0.262E+05}$
22.25.....	0.174E−03	0.149E−03 ± 0.739E−05	1.173 ± 0.058	$0.940E+05^{+0.508E+05}_{-0.350E+05}$
22.75.....	0.156E−03	0.120E−03 ± 0.126E−04	1.295 ± 0.136	$0.250E+06^{+0.867E+05}_{-0.690E+05}$
23.25.....	0.123E−03	0.773E−04 ± 0.172E−04	1.587 ± 0.353	$0.414E+06^{+0.160E+06}_{-0.138E+06}$
23.75.....	0.123E−03	0.492E−04 ± 0.180E−04	2.494 ± 0.914	$0.854E+06^{+0.388E+06}_{-0.363E+06}$

NOTES.—Col. (1): K-magnitude at center of 0.5 mag interval. Col. (2): Total area for sources in K-magnitude interval. Col. (3): Total effective area for sources in K-magnitude interval. Col. (4): Ratio of total to effective areas. Col. (5): Corrected counts mag^{-1} deg^{-2}.

However, the effective area to be used for the counts is weighted by the fractional detection at each depth,

$$S_{\rm eff}[m(j)] = \sum_{i=1}^{\min(i_{\rm max},\, j_{\rm max}-j)} N_{\rm pix}(i) df(j+i-1)\,, \qquad j < j_{\rm max}$$

and

$$S_{\rm eff}[m(j)] = \sum_{i=1}^{\min(i_{\rm max},\, j_{\rm max}-j+1)} N_{\rm pix}(i) df(j+i-1)\,, \qquad j = j_{\rm max}\,,$$

yielding the results in Table A3, column (3). The uncertainty in $S_{\rm eff}$ arises from the uncertainty in df. We define "Boost" to be $S_{\rm tot}/S_{\rm eff}$. The boost and its uncertainty are in column [4] of Table A3.

4. *The corrected counts* (A).—The corrected counts are calculated as

$$A = N/(S_{\rm eff}\, dm)\,,$$

where dm is the magnitude interval and $S_{\rm eff}$ is in square degrees such that A has units of counts mag^{-1} deg^{-2}. The corrected counts, A, in the original magnitude bins are listed in Table A3, column [5]. The uncertainties in A are a quadratic combination of the statistical counting errors (1 σ; Gehrels 1986) and the uncertainties in $S_{\rm eff}$. The corrected counts averaged over two of the above 0.5 mag bins, but stepped every 0.5 mag (1 original magnitude bin), are listed in Table A4, column (2). Note again that A is corrected to counts mag^{-1} deg^{-2}. The log of these last values are what are inserted into Table 1, as can be verified by inspection of column (3).

TABLE A4

AVERAGED COUNTS

K (1)	A (2)	log A (3)
18.5.....	$0.939E+04^{+0.124E+05}_{-0.607E+04}$	$3.973^{+0.365}_{-0.451}$
19.0.....	$0.000E+00^{+0.000E+00}_{-0.000E+00}$	...
19.5.....	$0.000E+00^{+0.000E+00}_{-0.000E+00}$	...
20.0.....	$0.990E+04^{+0.131E+05}_{-0.640E+04}$	$3.996^{+0.365}_{-0.451}$
20.5.....	$0.150E+05^{+0.146E+05}_{-0.817E+04}$	$4.176^{+0.295}_{-0.341}$
21.0.....	$0.431E+05^{+0.213E+05}_{-0.149E+05}$	$4.635^{+0.174}_{-0.185}$
21.5.....	$0.683E+05^{+0.260E+05}_{-0.195E+05}$	$4.835^{+0.140}_{-0.146}$
22.0.....	$0.773E+05^{+0.295E+05}_{-0.221E+05}$	$4.888^{+0.140}_{-0.146}$
22.5.....	$0.172E+06^{+0.470E+05}_{-0.387E+05}$	$5.235^{+0.105}_{-0.111}$
23.0.....	$0.332E+06^{+0.765E+05}_{-0.765E+05}$	$5.521^{+0.090}_{-0.114}$
23.5.....	$0.634E+06^{+0.193E+06}_{-0.193E+06}$	$5.802^{+0.116}_{-0.158}$

NOTES.—Col. (1): K-magnitude at center of 1 mag interval. Col. (2): Corrected counts mag^{-1} deg^{-2}. Col. (3): Log of corrected counts mag^{-1} deg^{-2}.

REFERENCES

Aragon-Salamanca, A., Ellis, R. S., Couch, W. J., & Carter D. 1993, MNRAS, 262, 764
Babul, A., & Ferguson, H. C. 1996, ApJ, 458, 100
Babul, A., & Rees, M. 1992, MNRAS, 255, 346
Bender, R., Bodo, Z., & Bruzual, G. 1996, ApJ, 463, 51
Bershady, M. A. 1995, AJ, 109, 87
Bershady, M. A., Hereld, M., Kron, R. G., Koo, D. C., Munn, J. A., & Majewski, S. R. 1994, AJ, 108, 870
Bershady, M. A., SubbaRao, M., Koo, D. C., Szalay, A., & Kron, R. G. 1998, in preparation
Bessell, M. S., & Brett, J. M. 1988, PASP, 100, 1134
Bruzual, A. G., & Charlot, S. 1993, ApJ, 405, 538
Casali, M., & Hawarden, T. 1992, JCMT-UKIRT Newsletter, 3, 33
Cáyon, L., Silk, J., & Charlot, S. 1996, ApJ, 467, L53
Colless, M., Schade, D., Broadhurst, T. J., & Ellis, R. S. 1994, MNRAS, 267, 1108
Cowie, L. L., Gardner, J. P., Hu, E. M., Songaila, A., Hodapp, K.-W., & Wainscoat, R. J. 1994, ApJ, 434, 114
Cowie, L. L., Gardner, J. P., Lilly, S. J., & McLean, I. 1990, ApJ, 360, L1
Cowie, L. L., Hu, E. M., & Songaila, A. 1995, AJ, 110, 1576
Dickinson, M. 1995, in ASP Conf. Proc. 86, Fresh Views on Elliptical Galaxies, ed. A. Buzzoni, A. Renzini, A. Serrano, (San Francisco: ASP), 283
Djorgovski, S. G., et al. 1995, ApJ, 438, L13
Dunlop, J., Peacock, J., Spinrad, H., Dey, A., Jiminez, R., Stern, D., & Windhorst, R. 1996, Nature, 381, 581
Ellis, R. S., & Allen, D. A. 1983, MNRAS, 203, 685
Ellis, R. S., Colless, M., Broadhurst, T., Heyl, J., & Glazebrook, K. 1996, MNRAS, 280, 235
Elston, R., Rieke, G., & Rieke, M. 1988, ApJ, 331, L77
Ferguson, H. C., & McGaugh, S. S. 1995, ApJ, 440, 470
Fukugita, M., Takahara, F., Yamashita, K., & Yoshii, Y. 1990, ApJ, 361, L1
Gardner, J. P., Cowie, L. L., & Wainscoat, R. J. 1993, ApJ, 415, L9
Gardner, J. P., Sharples, R. M., Carrasco, B. E., & Frenk, C. S. 1996, MNRAS, 282, L1
Gardner, J. P., Sharples, R. M., Frenk, C. S., & Carrasco, B. E. 1997, ApJ, 480, L99
Gehrels, N. 1986, ApJ, 303, 336
Giavalisco, M., Steidel, C. C., & Macchetto, F. D. 1996, ApJ, 470, 189
Glazebrook, K., Peacock, J. A., Miller, L., & Collins, C. A. 1995, MNRAS, 275, 169
Graham, J. R., & Dey, A. 1996, ApJ, 471, 720
Gronwall, C., & Koo, D. C. 1995, ApJ, 440, L1
Hall, P., & Mackay, C. D. 1984, MNRAS, 210, 979
Hogg, D. W., Neugebauer, G., Armus, L., Matthews, K., Pahre, M. A., Soifer, B. T., & Weinberger, A. J. 1997, AJ, 113, 2338
Holmberg, E. 1975, in Stars and Stellar Systems, vol. 9, Galaxies and the Universe, ed. A. Sandage, M. Sandage, & J. Kristian (Chicago: Univ. Chicago Press), 123
Hu, E. M., & Ridgeway, S. E. 1994, AJ, 107, 1303
Huchra, J. P. 1977, ApJ, 217, 928
Jarvis, J. F., & Tyson, J. A. 1981, AJ, 86, 476
Kauffmann, G., Charlot, S., & White, S. D. M. 1996, MNRAS, 283, L117
Koo, D. C. 1990, in ASP Conf. Proc. 10, Evolution of the Universe of Galaxies, ed. R. G. Kron (San Francisco: ASP), 268
Koo, D. C., & Kron, R. G. 1992, ARA&A, 30, 613
Koo, D. C., et al. 1996, ApJ, 469, 535
Kron, R. G. 1980, ApJS, 43, 305
———. 1995, in The Deep Universe, Saas Fee Advanced Course 23 (Berlin: Springer), 285
Kron, R. G., Koo, D. C., & Windhorst, R. A. 1985, A&A, 146, 38
Lilly, S. J., Cowie, L. L., & Gardner, J. P. 1991, ApJ, 369, 79
Lilly, S. J., Tresse, L., Hammer, F., Crampton, D., & Le Fevre, O. 1995, ApJ, 455, 108
Lin, H., Kirshner, R. P., Shectman, S. A., Landy, S. D., Oemler, A., Tucker, D. L., & Schecter, P. L. 1996, ApJ, 464, 60
Loveday, J., Peterson, B. A., Efstathiou, G., & Maddox, S. J. 1992, ApJ, 390, 338
Lowenthal, J. D., et al. 1997, ApJ, 481, 673
Marzke, R. O., Geller, M. J., Huchra, J. P., & Corwin, H. G., Jr. 1994, AJ, 108, 437
Matthews, K., & Soifer, B. T. 1994, in Infrared Astronomy with Arrays, ed. I. McLean (Dordrecht: Kluwer), 239
McCarthy, P. J. 1993, ARA&A, 31, 639
McGaugh, S. S., Bothun, G. D., & Schombert, J. M. 1995, ApJ, 110, 573
McLeod, B. A., Bernstein, G. M., Rieke, M. J., Tollestrup, E. V., & Fazio, G. G. 1995, ApJS, 96, 117
Metcalfe, N., Shanks, T., Fong, R., & Jones, L. R. 1991, MNRAS, 249, 498
Metcalfe, N., Shanks, T., Fong, R., & Roche, N. 1995, MNRAS, 273, 257
Mobasher, B., Sharples, R. M., & Ellis, R. S. 1993, MNRAS, 263, 560
Moustakas, L. A., Davis, M., Graham, J. R., Silk, J., Peterson, B. A., & Yoshii, Y. 1997, ApJ, 475, 445
Munn, J. A., Koo, D. C., Kron, R. G., Majewski, S. R., Bershady, M. A., & Smetanka, J. J. 1997, ApJS, 109, 45
Pahre, M. A., Djorgovski, S. G., & de Carvalho, R. R. 1996, ApJ, 456, L79
Petrosian, V. 1976, ApJ, 209, L1
Roche, N., Ratnatunga, K., Griffiths, R. E., Im, M., & Neuschaefer, L. 1996, MNRAS, 282, 1247
Saracco, P., Iovino, A., Garilli, B., Maccagni, D., & Chincarini, G. 1997, AJ, 114, 887
Schade, D., Carlberg, R. G., Yee, H. K. C., & López-Cruz, O. 1996, ApJ, 464, L63
Searle, L., Sargent, W. L. W., & Bagnuolo, W. G. 1973, ApJ, 179, 427
Smail, I., Hogg, D. W., Yan, L., & Cohen, J. G. 1995, ApJ, 449, L105
Soifer, B. T., et al. 1994, ApJ, 420, L1
Stanford, S. A., Eisenhardt, P. R. M., & Dickinson, M. 1995, ApJ, 450, 512
———. 1998, ApJ, 492, 261
Valdes, F. 1982, FOCAS User's Manual (Tuscon: NOAO)
Van Dokkum, P.G., & Franx, M. 1996, MNRAS, 281, 985
Wainscoat, R. J., & Cowie, L. L. 1992, AJ, 103, 332
Williams, R. E., et al. 1996, AJ, 112, 1335
Windhorst, R. A., Koo, D. C., & Spinrad, H. 1986, in Galaxy Distances and Deviations from Universal Expansion, ed. B. F. Madore & R. B. Tully (Dordrecht: Reidel), 197
Wirth, G. D., & Bershady, M. A. 1998, in preparation
Yoshii, Y., & Peterson, B. A. 1995, ApJ, 444, 15
Yoshii, Y., & Takahara, F. 1988, ApJ, 326, 1
Zepf, S. E. 1997, Nature, 390, 377